

First-quantized eigensolver for ground and excited states of electrons under a uniform magnetic field

Taichi Kosugi,^{1,2,*} Hirofumi Nishi,^{1,2} and Yu-ichiro Matsushita^{1,2,3}

¹*Laboratory for Materials and Structures, Institute of Innovative Research,
Tokyo Institute of Technology, Yokohama 226-8503, Japan*

²*Quemix Inc., Taiyo Life Nihombashi Building, 2-11-2, Nihombashi Chuo-ku, Tokyo 103-0027, Japan*

³*Quantum Material and Applications Research Center,
National Institutes for Quantum Science and Technology,
2-12-1, Ookayama, Meguro-ku, Tokyo 152-8552, Japan*

(Dated: July 3, 2023)

First-quantized eigensolver (FQE) is a recently proposed quantum computation framework for obtaining the ground state of an interacting electronic system based on probabilistic imaginary-time evolution. Here, we propose a method for introducing a uniform magnetic field to the FQE calculation. Our resource estimation demonstrates that the additional circuit responsible for the magnetic field can be implemented with a linear depth in terms of the number of qubits assigned to each electron. Hence, introduction of the magnetic field has no impact on the leading order of the entire computational cost. The proposed method is validated by numerical simulations of the ground and excited states employing filtration circuits for the energy eigenstates. We also provide a generic construction of the derivative circuits together with measurement-based formulae. As a special case of them, we can obtain the electric-current density in an electronic system to gain insights into the microscopic origin of the magnetic response.

I. INTRODUCTION

When an electronic system undergoes an external magnetic field, interesting phenomena that are never seen without the field are known to emerge. The most striking examples include the integer quantum Hall effect (IQHE) and the fractional QHE (FQHE) [1–5] appearing in two-dimensional systems. The IQHE originates from quantization of the in-plane motion of a single electron experiencing a perpendicular magnetic field leading to the discrete energy levels, called the Landau levels. In contrast, the FQHE exhibits rational fractional quantum numbers stemming from the correlated motion of multiple electrons under a perpendicular magnetic field.

Besides the exotic phenomena mentioned above, significant effects on practical applications of quantum systems are brought about by the coupling between an electronic system and an external magnetic field. The most important one among them is chemical shifts in the energy splittings of nuclear spins in a molecule or a solid [6]. Chemical shifts are mainly caused by the electron cloud partially shielding the external magnetic field near the nucleus. Although chemical shifts depend on the electronic environment and are smaller than the reference energy splittings in general, they are not negligible for realizing precise quantum information processing based on nuclear magnetic resonance (NMR) techniques [7–13].

Although the second-quantized formalism is widely adopted in the quantum computation community to determine the ground state of electronic systems, the first-quantized formalism [14–19] (or equivalently the

grid-based formalism) has attracted recent attention as a promising alternative. In particular, first-quantized eigensolver (FQE) [18], which is a framework of quantum chemistry based on the probabilistic imaginary-time evolution (PITE), provides nonvariational energy minimization with favorable scaling of computational resources compared to the second-quantized ones. Exhaustive search for optimal molecular geometries is also possible within FQE [20].

Given the importance of understanding and exploiting the coupling between an electronic system and an external magnetic field as discussed above, it is desirable to develop methods to incorporate external magnetic fields in the quantum computation of electronic systems. Although such a method has already been proposed for the second-quantized formalism [21], a first-quantized method remains lacking to our best knowledge. In this study, we employ the operator-splitting technique used by Watanabe and Tsukada [22] for classical computers to efficiently incorporate a uniform magnetic field in the FQE calculation. Our resource estimation demonstrates that the additional circuit responsible for the magnetic field can be implemented with a linear depth in terms of the number of qubits assigned to each electron, hence there is no impact on the leading order of the entire computational cost. In addition, we provide a generic construction of the derivative circuits, together with measurement-based formulae to extract the electric-current density that helps reveal the microscopic magnetic response of the target system. We also propose filtration circuits for eliminating undesired energy eigenstates based on the idea of Chan et al. [19]. Our new techniques are validated by performing FQE simulations for confined electronic systems under external magnetic fields.

* kosugi.taichi@gmail.com

II. METHODS

A. Brief review of PITE and first-quantized formalism

1. PITE circuits

The generic circuit for PITE [18] is shown in Fig. 1(a), which uses a single ancilla to implement probabilistically the nonunitary imaginary-time evolution (ITE) operator $\mathcal{M} = m_0 e^{-\mathcal{H}\Delta\tau}$ specified by the Hamiltonian \mathcal{H} of a target system and an imaginary-time step $\Delta\tau$. m_0 is an adjustable real parameter. PITE implements the desired nonunitary operation by resorting to a measurement. (See also Refs. [23, 24].) If the measurement outcome of the ancilla qubit is $|0\rangle$, the evolved state for an arbitrary input state $|\psi\rangle$ within the first order of $\Delta\tau$ has been successfully obtained. As seen in the circuit, each PITE step is implemented by using the real-time evolution (RTE) gates $U_{\text{RTE}}(\Delta t) = e^{-i\mathcal{H}\Delta t}$ for the renormalized real-time step $\Delta t \equiv s_1 \Delta\tau$, where $s_1 \equiv m_0/\sqrt{1-m_0^2}$ [18]. The PITE step has to be repeated successfully until the initial state becomes satisfactorily close to the ground state. The step width does not need to be constant during the iterations. For example, we can set it for the k th step to

$$\Delta\tau_k = (1 - e^{-k/\kappa})(\Delta\tau_{\text{max}} - \Delta\tau_{\text{min}}) + \Delta\tau_{\text{min}}, \quad (1)$$

so that it changes gradually from $\Delta\tau_{\text{min}}$ to $\Delta\tau_{\text{max}}$. κ determines the rate of change.

2. Encoding of many-particle wave functions

We explain here the encoding of wave function in real space for multiple particles whose dynamics is governed by the Schrödinger equation [14–19]. We do not take spin degrees of freedom into account for simplicity.

We discretize a finite interval in each of x, y , and z directions into equidistant points to which the computational bases of n qubits are assigned. Specifically, the x coordinates of the $N \equiv 2^n$ points are given by $x^{(k_x)} = k_x \Delta x$ ($k_x = 0, \dots, N-1$), where $\Delta x \equiv L/N$ is the grid step for an interval $[0, L]$ on the x axis. We assume that the simulation cell is a cube for simplicity. The y and z coordinates are similarly given by $y^{(k_y)} = k_y \Delta x$ and $z^{(k_z)} = k_z \Delta x$, respectively. We assign each computational basis $|\mathbf{k}\rangle_{3n} \equiv |k_x\rangle_n \otimes |k_y\rangle_n \otimes |k_z\rangle_n$ of the $3n$ qubits to each of the position eigenstates of each particle: $\hat{x}|\mathbf{k}\rangle_{3n} = x^{(k_x)}|\mathbf{k}\rangle_{3n}$, where \hat{x} is the position operator for x direction. We also write the eigenstate of x position as $|x^{(k_x)}\rangle$. The position operators and eigenstates for y and z directions are defined similarly. Let us consider a system made up of n_{par} particles and encode its wave function $\Psi(\mathbf{r}_0, \dots, \mathbf{r}_{n_{\text{par}}-1})$ by using $3nn_{\text{par}}$ qubits. We assume that the wave function is normalized to be unity

when it is integrated over the simulation cell. The coefficient of each computational basis thus represents the many-particle wave function as

$$|\Psi\rangle = \Delta V^{n_{\text{par}}/2} \sum_{\mathbf{k}_0, \dots, \mathbf{k}_{n_{\text{par}}-1}} \Psi(\mathbf{r}^{(\mathbf{k}_0)}, \dots, \mathbf{r}^{(\mathbf{k}_{n_{\text{par}}-1})}) \cdot |\mathbf{k}_0\rangle_{3n} \otimes \dots \otimes |\mathbf{k}_{n_{\text{par}}-1}\rangle_{3n}, \quad (2)$$

where we introduced the volume element $\Delta V \equiv (L/N)^3$ so that the normalization condition for the many-qubit state $\langle\Psi|\Psi\rangle = 1$ is satisfied. In what follows, we assume that the wave function has the periodicity of simulation cell for each direction of each position coordinate. We further assume that the initial many-particle state in an FQE calculation has already been symmetrized or antisymmetrized under exchange of any pair of particles according to the statistics [25, 26].

As the canonical counterpart of the discretized positions, we define the N discrete momenta of a particle for each direction $p^{(\tilde{s})} \equiv \tilde{s}\Delta p$ ($\tilde{s} = -N/2, -N/2 + 1, \dots, N/2 - 1$) with the momentum step $\Delta p \equiv 2\pi/L$ in reciprocal space. The tilde symbol for an integer j means $\tilde{j} \equiv j - N/2$ in what follows. We define the momentum eigenstate specified by three integers s_x, s_y , and s_z as the Fourier transform of the position eigenstates:

$$|\mathbf{p}^{(\tilde{\mathbf{s}})}\rangle \equiv \frac{1}{N^{3/2}} \sum_{k_x=0}^{N-1} \sum_{k_y=0}^{N-1} \sum_{k_z=0}^{N-1} \exp(i\mathbf{p}^{(\tilde{\mathbf{s}})} \cdot \mathbf{r}^{(\mathbf{k})}) |\mathbf{k}\rangle_{3n}. \quad (3)$$

$|\mathbf{p}^{(\tilde{\mathbf{s}})}\rangle$ is also the eigenstate of $\hat{T}_{0\nu} \equiv \hat{p}_\nu^2/(2m)$ ($\nu = x, y, z$) for each direction belonging to the discrete kinetic energy $E_{\text{kins}} \equiv \tilde{s}^2(\Delta p)^2/(2m)$. By defining the kinetic-phase gate $U_{\text{kin}}(\Delta t)$ for n qubits such that it acts on a computational basis $|j\rangle_n$ as $U_{\text{kin}}(\Delta t)|j\rangle_n = \exp(-iE_{\text{kin}j}\Delta t)|j\rangle_n$, the n -qubit RTE operator generated by $\hat{T}_{0\nu}$ can be implemented as

$$\text{CQFT} \cdot U_{\text{kin}}(\Delta t) \cdot \text{CQFT}^\dagger = e^{-i\hat{T}_{0\nu}\Delta t} \quad (4)$$

for each direction, where CQFT is the centered quantum Fourier transform [18, 27, 28]. The consistent adoption of the range $[0, L]$ for spatial discretization and CQFT is just a matter of convention. In fact, the combination of a range $[-L/2, L/2]$ and the ordinary QFT [29] is possible in formulating the first-quantized approach [19].

B. FQE for a particle under a uniform magnetic field

1. Hamiltonian

In the present study, we focus on the techniques for incorporating a uniform static magnetic field into the FQE framework. We consider a single spinless quantum mechanical particle in three dimensional space. It has a

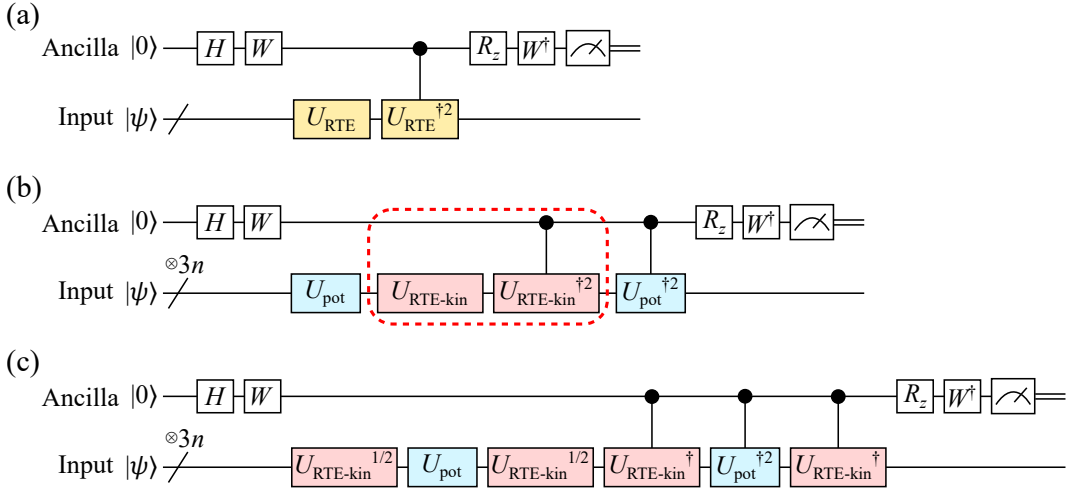


FIG. 1. (a) PITE circuit for a generic system governed by its Hamiltonian \mathcal{H} . It contains the RTE gate $U_{\text{RTE}} \equiv \exp(-i\mathcal{H}\Delta t)$ for an imaginary-time step $\Delta\tau$ and $\Delta t \equiv s_1\Delta\tau$. $R_z \equiv R_z(-2\theta_0)$ is the single-qubit z -rotation. For the definition of θ_0 and W , see Ref. [18] H is the Hadamard gate. (b) and (c) are the circuits for a single particle when the TV and TVT splittings for \mathcal{H} are adopted, respectively.

mass m and a charge q subject to an external potential V and an external magnetic field \mathbf{B} . The Hamiltonian \mathcal{H} is the sum of the kinetic part

$$\hat{T} = \frac{1}{2m} \left(\hat{\mathbf{p}} - \frac{q}{c} \mathbf{A}(\hat{\mathbf{r}}) \right)^2 \quad (5)$$

and the potential part $\hat{V} \equiv V(\hat{\mathbf{r}})$. $\hat{\mathbf{r}}$ is the position operator and $\hat{\mathbf{p}}$ is the canonical-momentum operator. The vector potential is defined such that its rotation gives the magnetic field: $\mathbf{B}(\mathbf{r}) = \nabla \times \mathbf{A}(\mathbf{r})$. For constructing the PITE circuit, we have to implement the RTE operator $U_{\text{RTE}}(\Delta t) = e^{-i(\hat{T}+\hat{V})\Delta t}$ for the $3n$ qubits by employing the Suzuki–Trotter formula. We examine in this study the following two splitting patterns, that is, the first-order splitting

$$U_{\text{RTE}}(\Delta t) = e^{-i\hat{T}\Delta t} e^{-i\hat{V}\Delta t} + \mathcal{O}(\Delta t^2), \quad (6)$$

which we call the TV splitting, and the second-order splitting

$$U_{\text{RTE}}(\Delta t) = e^{-i\hat{T}\Delta t/2} e^{-i\hat{V}\Delta t} e^{-i\hat{T}\Delta t/2} + \mathcal{O}(\Delta t^3), \quad (7)$$

which we call the TVT splitting. From the kinetic-evolution operator $U_{\text{RTE-kin}}(\Delta t) \equiv e^{-i\hat{T}\Delta t}$ and the potential-evolution operator $U_{\text{pot}}(\Delta t) \equiv e^{-i\hat{V}\Delta t}$, the PITE circuit for the TV splitting is constructed as shown in Fig. 1(b), while that for the TVT splitting is shown in Fig. 1(c).

2. Kinetic evolution

If there were no magnetic field, the kinetic-evolution for the x , y , and z directions in $U_{\text{RTE-kin}}(\Delta t)$ could be

decoupled. This is not the case for the system we are considering. We can assume without loss of generality that the magnetic field is along the z direction and it is generated by the Landau gauge: $\mathbf{A}(\mathbf{r}) = Bx\mathbf{e}_y$. With this choice of vector potential, the kinetic evolution operator is decomposed as follows:

$$U_{\text{RTE-kin}}(\Delta t) = \exp \left(-\frac{i\Delta t}{2m} \left(\hat{p}_y - \frac{qB}{c} \hat{x} \right)^2 \right) e^{-i\hat{T}_{0x}\Delta t} e^{-i\hat{T}_{0z}\Delta t} + \mathcal{O}(\Delta t^2), \quad (8)$$

where we used the first-order Suzuki–Trotter formula. The term of the form $\hat{p}_y\hat{x} - \hat{x}\hat{p}_y$ involved in the exponent for x and y directions is unfavorable for the implementation as a gate sequence. Therefore we use the identity $e^{-ia(\hat{p}_y-b)^2} = e^{ib\hat{y}} e^{-ia\hat{p}_y^2} e^{-ib\hat{y}}$ for arbitrary real a and b independent of y to split the evolution for y direction exactly as

$$\exp \left(-\frac{i\Delta t}{2m} \left(\hat{p}_y - \frac{qB}{c} \hat{x} \right)^2 \right) = U_{\text{mag}} e^{-i\hat{T}_{0y}\Delta t} U_{\text{mag}}^\dagger, \quad (9)$$

where

$$U_{\text{mag}} \equiv e^{iqB\hat{x}\hat{y}/c} \quad (10)$$

is the magnetic-phase gate for the $2n$ qubits, independent of the time step. The splitting in Eq. (9) is favorable since the position and momentum operators are decoupled. This splitting was used by Watanabe and Tsukada [22] for simulations on a classical computer to integrate the real-time-dependent Schrödinger equation for an electron under a magnetic field. By substituting Eq. (9) into

Eq. (8), we find the easy-to-implement expression of the evolution operator:

$$U_{\text{RTE-kin}}(\Delta t) = U_{\text{mag}} e^{-i\hat{T}_{0y}\Delta t} U_{\text{mag}}^\dagger e^{-i\hat{T}_{0x}\Delta t} e^{-i\hat{T}_{0z}\Delta t} + \mathcal{O}(\Delta t^2), \quad (11)$$

which is adopted in the present study.

3. Gate sequences for PITE circuits

We can now find the gate sequences in the PITE circuit for the particle under the magnetic field according to the splitting patterns. As seen in Figs. 1(b) and (c), $U_{\text{RTE-kin}}$ in the PITE circuit can appear as a controlled gate. It is easily confirmed that $U_{\text{RTE-kin}}(\Delta t)$ in Eq. (11) controlled by the ancilla can be implemented as a gate sequence in Fig. 2(a), where only the kinetic-phase gates in Eq. (4) are controlled. For the TV splitting of the total Hamiltonian, the dashed region in Fig. 1(b) is implemented as shown in Fig. 2(b). The PITE circuit for the TVT splitting is also constructed similarly (not shown). It should be noted here that, whatever splitting pattern is adopted, the error of the whole PITE calculation is $\mathcal{O}(\Delta t^2)$ since the original circuit in Fig. 1(a) is correct within the first order of Δt .

The reason for the TV splitting having been adopted by us instead of VT splitting is now clear. If the latter was adopted, the cancellation of the parts of $U_{\text{RTE-kin}}(\Delta t)$ and $U_{\text{RTE-kin}}(\Delta t)^\dagger$ would not have occurred and the circuits would be deeper than those in Figs. 2(b). It is similarly the case with the reason for the adoption of TVT splitting instead of VTV splitting.

C. Implementation of phase gates

1. Kinetic-phase gate

The kinetic-phase gate can be implemented by the technique proposed by Benenti and Strini [30]. We describe the implementation briefly here in order for this paper to be self-contained.

We consider here a one-dimensional system for simplicity where n qubits are used per particle for encoding the wave function. By defining $e_{\text{kin}} \equiv \Delta p^2/(2m)$ and the single-qubit phase gate

$$Z_{\text{kin}}(u) \equiv |0\rangle\langle 0| + \exp(iue_{\text{kin}}\Delta t) |1\rangle\langle 1| \quad (12)$$

specified by a real parameter u , the kinetic-phase operator can be written as

$$U_{\text{kin}}(\Delta t) = e^{-iN^2 e_{\text{kin}} \Delta t/4} \left(\prod_{\ell=0}^{n-1} \overbrace{Z_{\text{kin}}(2^\ell(N-2^\ell))}^{\text{On } \ell\text{th qubit}} \right) \cdot \prod_{\ell=0}^{n-1} \prod_{\ell' < \ell} C_{\ell, \ell'} Z_{\text{kin}}(-2^{\ell+\ell'+1}), \quad (13)$$

where $C_{\ell, \ell'} Z_{\text{kin}}$ represents the Z_{kin} gate on the ℓ' th qubit controlled by the ℓ th qubit. For the derivation of Eq. (13), see Appendix A. We must not omit the overall phase factor in the expression since the kinetic-phase gate in the PITE circuit can be controlled by the ancilla. The gate sequence that implements $U_{\text{kin}}(\Delta t)$ for $n = 4$ is shown in Fig. 3(a) as an example.

2. Magnetic-phase gate

Here we describe the implementation of the magnetic-phase gate defined in Eq. (10). From $\mu \equiv qB/c$, we define the single-qubit phase gate

$$Z_{\text{mag}}^{(\ell)} \equiv |0\rangle\langle 0| + \exp(i2^\ell \mu \Delta x^2) |1\rangle\langle 1| \quad (14)$$

specified by an integer ℓ . The magnetic-phase operator can then be written as

$$U_{\text{mag}} = \prod_{d=0}^{n-1} \prod_{\ell=0}^{n-1} C_{\ell, \ell'} Z_{\text{mag}}^{(\ell+\ell')} |_{\ell'=\ell+d \bmod n}, \quad (15)$$

where $C_{\ell, \ell'} Z_{\text{mag}}^{(\ell+\ell')}$ represents the $Z_{\text{mag}}^{(\ell+\ell')}$ gate on the ℓ' th qubit for the y position coordinate controlled by the ℓ th qubit for the x position coordinate. For the derivation of Eq. (15), see Appendix B. Equation (15) enables one to implement U_{mag} as a depth- $\mathcal{O}(n)$ circuit since, for a fixed d , the controlled single-qubit phase gates can be parallelized. The gate sequence that implements U_{mag} for $n = 4$ is shown in Fig. 3(b) as an example.

We can also adopt the shifted Landau gauge $\mathbf{A}(\mathbf{r}) = (x - x_g)B\mathbf{e}_y$ with an arbitrary x_g , leading to the same magnetic field as the unshifted one. The magnetic-phase gate in such a case is $U_{\text{mag}} = e^{iqB(\hat{x}-x_g)\hat{y}/c}$ instead of Eq. (10), which requires us to append the circuit implementation of $e^{-iqBx_g\hat{y}/c}$ to that in Eq. (15). Since the depth of the additional circuit is $\mathcal{O}(1)$, the scaling of the entire magnetic-phase circuit is the same as for the unshifted gauge.

D. Computational cost

In this subsection, we compare the splitting patterns for the RTE operator to estimate their computational cost for PITE calculations.

For a single particle in three-dimensional space, Table I shows the numbers of calls of major subroutines in a single PITE step [see Figs. 1(b) and (c)] for the two splitting patterns with or without a magnetic field. The call number of U_{pot} is independent of the presence of a magnetic field and the order (TV or TVT) of splitting. The call number of U_{mag} is smaller than those of QFT and U_{kin} . Furthermore, as stated above, U_{mag} admits the depth- $\mathcal{O}(n)$ implementation, whereas QFT and U_{kin} require $\mathcal{O}(n^2)$ depths. The operations of U_{mag} thus does

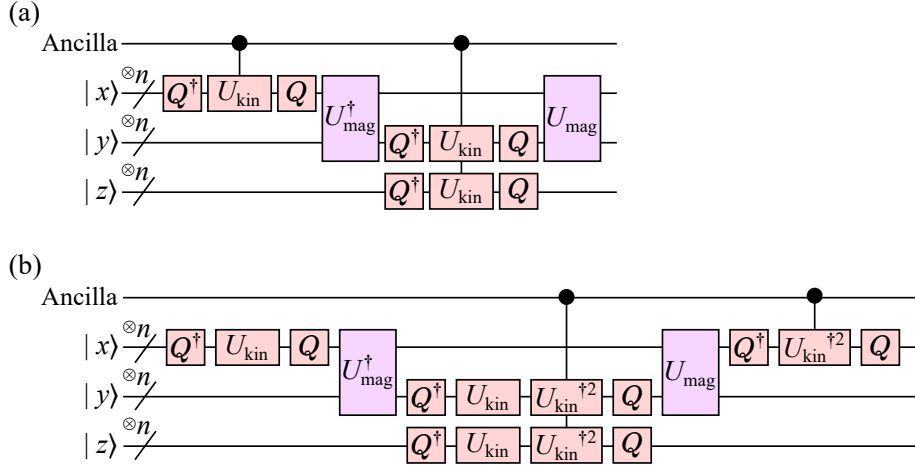


FIG. 2. (a) Gate sequence that implements the controlled $U_{\text{RTE-kin}}(\Delta t)$ in Eq. (11). Q represents the CQFT operator. $U_{\text{kin}} \equiv U_{\text{kin}}(\Delta t)$ is used in the figure. (b) Implementation of the dashed region in Fig. 1(b) for the TV splitting.

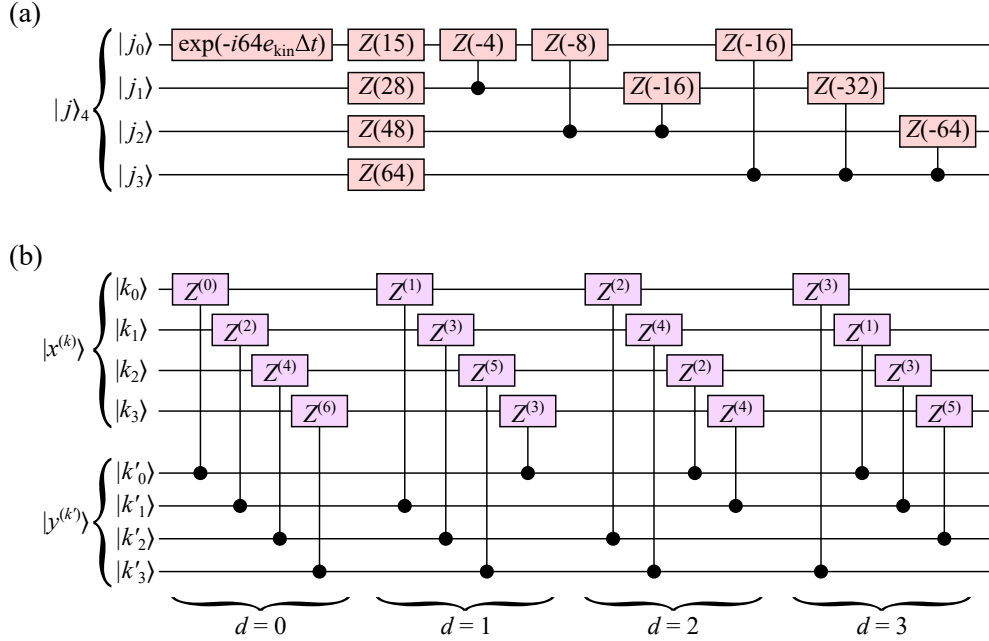


FIG. 3. (a) Gate sequence that implements the kinetic-phase gate $U_{\text{kin}}(\Delta t)$ for $n=4$. $Z(u)$ in this figure represents $Z_{\text{kin}}(u)$ defined in Eq. (12). (b) Depth- $\mathcal{O}(n)$ gate sequence that implements the magnetic-phase gate U_{mag} for $n=4$. $Z^{(\ell)}$ in this figure represents $Z_{\text{mag}}^{(\ell)}$ defined in Eq. (14). The values of d correspond to those in Eq. (15).

not contribute to the scaling of total depth with respect to n .

In a practical system where n_e electrons interact with each other, particle-wise parallelization of U_{mag} and QFT operations is possible in a single PITE step, whereas that of U_{kin} , U_{pot} , and the phase gate U_{int} for the interactions [18] is not possible due to the ancillary qubit. Therefore U_{mag} does not contribute to the scaling of total depth with respect to n_e . The circuit for a single PITE step used in such an FQE calculation for a molecule is depicted in

Fig. 4. This circuit is a many-electron extension of that in Fig. 1(b) and involves the TV splitting circuit in Fig. 2(b) for each electron. This is also a nonzero-magnetic-field version of the circuit in Fig. 2(b) in Ref. [18]. The PITE circuit for a molecule using the TVT splitting can also be constructed similarly (not shown). Also, the introduction of a magnetic field does not increase the call numbers of U_{kin} , U_{pot} , and U_{int} . In short, the introduction of a magnetic field to an interacting electronic system does not lead to a large increase in computational cost. This is

TABLE I. Numbers of calls of major subroutines in a single PITE step for a single particle. Those in parentheses represent the call numbers of controlled subroutines.

Splitting pattern	QFT	U_{kin}	U_{mag}	U_{pot}
$B = 0$				
TV	6	6 (3)	0	2 (1)
TVT	18	12 (6)	0	2 (1)
$B \neq 0$				
TV	8	6 (3)	2	2 (1)
TVT	20	12 (6)	6	2 (1)

also the case where an external magnetic field is introduced for the geometry optimization within FQE [20].

Here we mention the comparison with second-quantized approaches. For incorporating an external static magnetic field into a second-quantized Hamiltonian in quantum chemistry on a classical computer, one often employs the one-electron atomic orbitals that take the presence of the vector potential into account [31, 32]. The one- and two-electron integrals between them are calculated for the parameters in the Hamiltonian. Once it is constructed, the classical computation for finding the ground state for the fixed molecular geometry proceeds similarly to no-magnetic-field cases. The Hamiltonian can also be adopted for a second-quantized approach on a quantum computer. The advantages and disadvantages of the first- and second-quantized approaches over each other in no-magnetic-field cases [18] are inherited to nonzero-magnetic-field cases in principle. For example, a second-quantized approach requires much less number of qubits for encoding electronic orbitals in general, while a first-quantized approach requires qubits for sufficiently many grid points for each electron. On the other hand, a second-quantized approach requires $\mathcal{O}(n_e^5)$ classical computation for the two-electron integrals between the molecular orbitals before the quantum computation starts. In addition, the interaction terms in the Hamiltonian demand $\mathcal{O}(n_e^4)$ quantum computational time. Our first-quantized approach is free from both of them.

E. Obtaining electric-current density via measurements

1. One-electron density matrix and electric-current density

For the n_e -electron state $|\Psi\rangle$ represented by Eq. (2), the reduced density operator [29] for a single electron is calculated by tracing out the degrees of freedom of $n_e - 1$ electrons from the total density operator:

$$\begin{aligned} \rho_{\text{one}} &= \text{Tr}_{n_e-1} |\Psi\rangle\langle\Psi| \\ &= \frac{\Delta V}{n_e} \sum_{\mathbf{k}, \mathbf{k}'} \gamma(\mathbf{r}^{(\mathbf{k})}, \mathbf{r}^{(\mathbf{k}')}) |\mathbf{k}\rangle\langle\mathbf{k}'|_{3n}, \end{aligned} \quad (16)$$

where

$$\begin{aligned} \gamma(\mathbf{r}, \mathbf{r}') &\equiv n_e \int d^3\mathbf{r}_1 \cdots d^3\mathbf{r}_{n_e-1} \Psi(\mathbf{r}, \mathbf{r}_1, \dots, \mathbf{r}_{n_e-1}) \\ &\quad \cdot \Psi(\mathbf{r}', \mathbf{r}_1, \dots, \mathbf{r}_{n_e-1})^* \\ &= n_e \Delta V^{n_e-1} \sum_{\mathbf{k}_1, \dots, \mathbf{k}_{n_e-1}} \Psi(\mathbf{r}, \mathbf{r}^{(\mathbf{k}_1)}, \dots, \mathbf{r}^{(\mathbf{k}_{n_e-1})}) \\ &\quad \cdot \Psi(\mathbf{r}', \mathbf{r}^{(\mathbf{k}_1)}, \dots, \mathbf{r}^{(\mathbf{k}_{n_e-1})})^* \end{aligned} \quad (17)$$

is the reduced density matrix [33] for a single electron, or equivalently the one-electron density matrix (1DM), in position representation. Its normalization condition we have adopted is the conventional one in condensed-matter physics. Specifically, the diagonal components give the electron density $\rho(\mathbf{r})$ to satisfy

$$\int d\mathbf{r} \gamma(\mathbf{r}, \mathbf{r}) = \Delta V \sum_{\mathbf{k}} \rho(\mathbf{r}^{(\mathbf{k})}) = n_e, \quad (18)$$

which leads to the normalization condition $\text{Tr} \rho_{\text{one}} = 1$ for Eq. (16), the conventional one in quantum information processing.

It is known that the paramagnetic electric-current density as a function of position can be calculated from the 1DM as [33]

$$\mathbf{j}_{\text{para}}(\mathbf{r}) = \frac{(-e)}{m} \text{Im} \left. \frac{\partial \gamma(\mathbf{r}, \mathbf{r}')}{\partial \mathbf{r}} \right|_{\mathbf{r}'=\mathbf{r}} \quad (19)$$

and the diamagnetic electric-current density can be calculated as

$$\mathbf{j}_{\text{dia}}(\mathbf{r}) = -\frac{(-e)^2}{mc} \rho(\mathbf{r}) \mathbf{A}(\mathbf{r}). \quad (20)$$

The factor $-e < 0$ in Eqs. (19) and (20) comes from the negative electron charge. It is noted that the paramagnetic and diamagnetic current densities are solely gauge dependent, whereas the total current density $\mathbf{j}(\mathbf{r}) = \mathbf{j}_{\text{para}}(\mathbf{r}) + \mathbf{j}_{\text{dia}}(\mathbf{r})$ is gauge invariant to admit physically meaningful interpretations [33].

2. Circuits and measurement-based formula

The electric-current density provides insights for understanding the microscopic origin of the response of a target system to an external magnetic field such as the shielding due to the electron clouds [34, 35]. We describe below how the electric-current density can be obtained from measurements on qubits that encode the wave function in real space.

The electron density can be obtained simply by measuring $3n$ qubits in $|\Psi\rangle$ since the electrons are indistinguishable. Specifically, the electron density at $\mathbf{r}^{(\mathbf{k})}$ is related to the probability for observing $|\mathbf{k}\rangle_{3n}$ for an arbitrary electron among n_e as

$$\rho(\mathbf{r}^{(\mathbf{k})}) = \frac{n_e}{\Delta V} \mathbb{P}_{\mathbf{k}}. \quad (21)$$

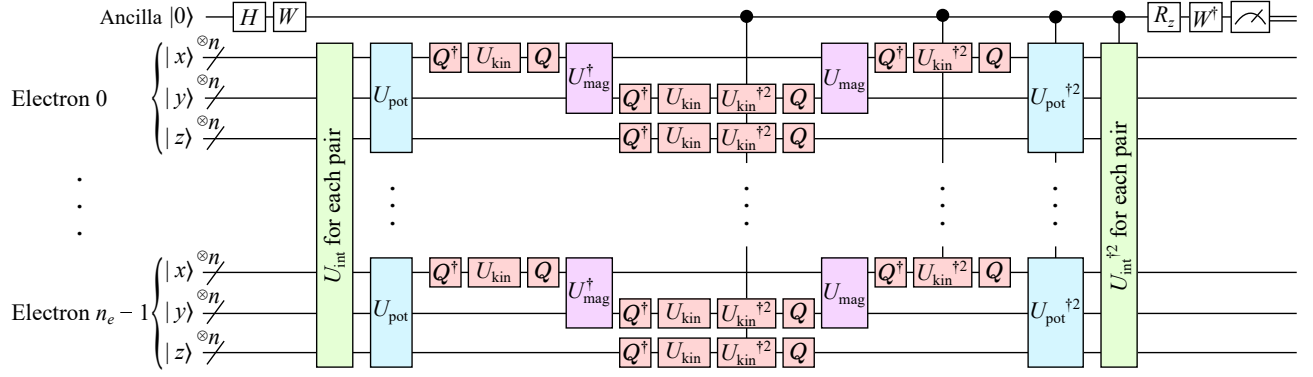


FIG. 4. Circuit for a single PITE step used in an FQE calculation for n_e interacting electrons under a static magnetic field. This circuit involves the TV splitting circuit in Fig. 2(b) for each electron.

The electron density constructed via repeated measurements and Eq. (20) allow us to get the diamagnetic current density.

In contrast to the diamagnetic current density, obtaining the paramagnetic current density requires some trick due to the presence of the position derivative of 1DM. [See Eq. (19)] For obtaining the x component of paramagnetic current density, we introduce the circuit $\mathcal{C}_{\text{para},x}(d)$, as shown in Fig. 5. This circuit comes from the generic method for obtaining the derivative distributions of a complex function described in Appendix C. This circuit acts on the ancilla and the $3n$ qubits for an arbitrary electron among the n_e electrons. $U_{\text{shift}}(d)$ is a phase gate specified by an integer d which acts on the computational basis as $|j\rangle_n \mapsto \exp(-i2\pi dj/N)|j\rangle_n$ ($j = 0, \dots, N-1$). The circuit ends up with a measurement on the ancilla and the $3n$ qubits responsible for the single electron with ignoring the other qubits.

We use the circuits $\mathcal{C}_{\text{para},x}(d)$ and $\mathcal{C}_{\text{para},x}(-d)$ for obtaining the desired quantity. Specifically, we have the measurement-based formula

$$j_{\text{para},x}(\mathbf{r}^{(\mathbf{k})}) = \frac{(-e)}{m} \frac{1}{2d\Delta x} \left(\frac{2n_e}{\Delta V} (-\mathbb{P}_{\mathbf{k}0}(-d) + \mathbb{P}_{\mathbf{k}0}(d)) + \frac{\rho(\mathbf{r}^{(\mathbf{k})} + d\Delta x \mathbf{e}_x) - \rho(\mathbf{r}^{(\mathbf{k})} - d\Delta x \mathbf{e}_x)}{2} \right) + \mathcal{O}(\Delta x^2), \quad (22)$$

where $\mathbb{P}_{\mathbf{k}0}(\pm d)$ is the probability for observing $|\mathbf{k}\rangle_{3n}$ for the electron and $|0\rangle$ for the ancilla when a measurement is performed for the $\mathcal{C}_{\text{para},x}(\pm d)$ circuit. Equation (22) enables one to calculate the x component of paramagnetic current density via repeated measurements within the first order of Δx . For the derivation of this equation, see Appendix D. The circuits $\mathcal{C}_{\text{para},y}(d)$ and $\mathcal{C}_{\text{para},z}(d)$ for obtaining the y and z components, respectively, can also be constructed similarly.

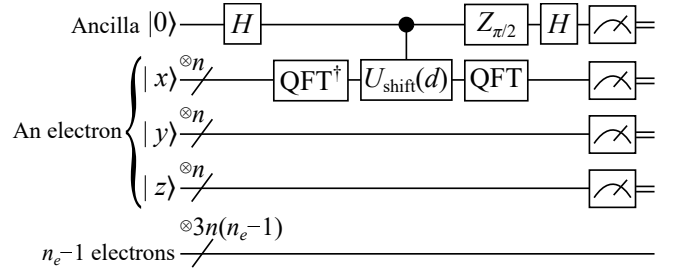


FIG. 5. $(3n+1)$ -qubit circuit $\mathcal{C}_{\text{para},x}(d)$ for obtaining the x component of paramagnetic electric-current density $j_{\text{para}}(\mathbf{r})$. $Z_{\pi/2} = |0\rangle\langle 0| + e^{i\pi/2}|1\rangle\langle 1|$ is a single-qubit phase gate. The measurements are performed on the ancillary qubit and the $3n$ qubits responsible for an arbitrary electron among n_e .

F. Filtration circuits for excited states

Since any kind of ITE approach lets the lowest-energy eigenstate in an initial state survive imaginary-time lapses while it forces the other eigenstates to diminish, it is desirable to develop techniques that remove a specific energy eigenstate from the initial state [19]. To this end, we describe below two circuits for probabilistic filtration, which require only the estimated energy eigenvalues and does not require the eigenstates. There can often be a case in which we have estimated lowest energy eigenvalues via some reliable approaches such as those related to Krylov subspace [36–39], without having obtained the eigenstates as qubits.

We should point out here that, while the schemes below are for killing a single undesirable state via a single measurement, Meister and Benjamin [40] have already proposed elaborate schemes for killing multiple undesirable states via consecutive measurements based on the knowledge of energy levels within a target range.

1. First-order filtration

For an input n -qubit state $|\psi\rangle$ whose Hamiltonian is \mathcal{H} , we construct the first-order probabilistic filtration circuit $\mathcal{C}_{\text{filt1}}^{(\lambda)}$ for a target elimination energy λ , as shown in Fig. 6(a). This circuit is essentially the same as the one proposed by Chan et al. [19] The real-time step Δt_f is an adjustable parameter. The state of $(n+1)$ -qubit system immediately before the measurement on the ancilla is

$$\begin{aligned} & \frac{e^{-i\lambda\Delta t_f/2} - e^{i(\lambda/2 - \mathcal{H})\Delta t_f}}{2} |\psi\rangle \otimes |0\rangle \\ & + \frac{e^{-i\lambda\Delta t_f/2} + e^{i(\lambda/2 - \mathcal{H})\Delta t_f}}{2} |\psi\rangle \otimes |1\rangle. \end{aligned} \quad (23)$$

Let us consider a practical situation in which the observer wants to remove the ground state $|\phi_0\rangle$ from the input state with knowing an estimated ground state energy \tilde{E}_0 to obtain the first excited state $|\phi_1\rangle$ in subsequent procedures. The estimated energy can have an error δE_0 from the true energy eigenvalue E_0 as $\tilde{E}_0 = E_0 + \delta E_0$ and the observer uses $\mathcal{C}_{\text{filt1}}^{(\tilde{E}_0)}$. Such errors can stem from various origins, e.g., a finite number of measurements to estimate the energy eigenvalue or a dephasing process the qubits undergo or classical noises disturbing the circuit parameters. The explanations of filtration techniques below, however, are not affected by what the origins are. It is clear from Eq. (23) that, if the error is zero and the measurement outcome is $|0\rangle$, the resultant n -qubit state, which we call the success state in what follows, does not contain $|\phi_0\rangle$.

If the observer has an estimated energy \tilde{E}_1 of the first excited state that can have an error as well as the ground state, it may be appropriate to set the time step Δt_f to

$$\Delta t_1 \equiv \frac{\pi}{\tilde{E}_1 - \tilde{E}_0}. \quad (24)$$

For this time step, the weight of $|\phi_1\rangle$ in the success state acquires a factor $\sin^2(\pi/2) = 1$ if the error δE_1 is zero. Specifically, by expanding the input state in terms of the energy eigenstates as $|\psi\rangle = \sum_k c_k |\phi_k\rangle$, the unnormalized success state is written as (see Appendix E)

$$\sum_k i c_k \exp\left(-i \frac{\pi E_k}{2(\tilde{E}_1 - \tilde{E}_0)}\right) \sin \frac{\pi(E_k - \tilde{E}_0)}{2(\tilde{E}_1 - \tilde{E}_0)} |\phi_k\rangle, \quad (25)$$

where the amplitude of ground state is $\mathcal{O}(\delta E_0)$. The relative weight of the ground state compared to the first excited state in the success state is, from Eq. (25),

$$r_{\text{filt1}} \equiv \left| \frac{c_0}{c_1} \right|^2 \frac{\sin^2 \frac{\pi \bar{\delta} E_0}{2(1 + \bar{\delta} E_1 - \bar{\delta} E_0)}}{\cos^2 \frac{\pi \bar{\delta} E_1}{2(1 + \bar{\delta} E_1 - \bar{\delta} E_0)}}, \quad (26)$$

where $\bar{\delta} E_k \equiv \delta E_k / (E_1 - E_0)$ ($k = 0, 1$) is the relative error with respect to the energy gap.

After the first-order filtration described above, the PITE steps begin from the n -qubit state having a possibly small weight of the ground state to eliminate the second and higher excited states. In order for the resultant state after n_{steps} PITE steps to be close to the first excited state, the relative weight $\exp(n_{\text{steps}}(E_1 - E_0)\Delta\tau)r_{\text{filt1}}$ of the ground state has to be still small, say ε . The condition for this requirement is

$$\begin{aligned} n_{\text{steps}}\Delta\tau < \frac{1}{E_1 - E_0} \left(\ln \varepsilon + 2 \ln \left| \frac{c_1}{c_0} \right| \right. \\ \left. + 2 \ln \left| \frac{\cos \frac{\pi \bar{\delta} E_1}{2(1 + \bar{\delta} E_1 - \bar{\delta} E_0)}}{\sin \frac{\pi \bar{\delta} E_0}{2(1 + \bar{\delta} E_1 - \bar{\delta} E_0)}} \right| \right) \equiv \tau_{\text{ub1}}, \end{aligned} \quad (27)$$

which imposes the upper bound τ_{ub1} on the allowed total imaginary-time lapse. In particular, when the errors are smaller than the energy gap ($\bar{\delta} E_0 \ll 1$ and $\bar{\delta} E_1 \ll 1$), the upper bound is approximated as

$$\tau_{\text{ub1}} \approx \frac{1}{E_1 - E_0} \left(\ln \frac{4\varepsilon}{\pi^2} + 2 \ln \left| \frac{c_1}{c_0} \right| + 2 \ln \frac{1}{|\bar{\delta} E_0|} \right). \quad (28)$$

This expression tells us that, for a fixed tolerance ε , a better initial state ($|c_1| \gg |c_0|$) and a better estimation for the ground state energy ($|\delta E_0| \ll |E_1 - E_0|$) lead to a larger upper bound. When the lapse exceeds the upper bound, we will have to apply the filtration again to get the target excited state.

2. Second-order filtration

By introducing two ancillae $|q_1\rangle \otimes |q_0\rangle$, we can construct the second-order probabilistic filtration circuit $\mathcal{C}_{\text{filt2}}^{(\lambda)}$ for the input $|\psi\rangle$, as shown in Fig. 6(b). The state of $(n+2)$ -qubit system immediately before the measurement on the ancillae is

$$\begin{aligned} & \cos^2 \frac{(\mathcal{H} - \lambda)\Delta t_f}{2} |\psi\rangle \otimes |0\rangle \otimes |0\rangle \\ & + \sin^2 \frac{(\mathcal{H} - \lambda)\Delta t_f}{2} |\psi\rangle \otimes |1\rangle \otimes |0\rangle \\ & + \frac{i}{2} \sin((\mathcal{H} - \lambda)\Delta t_f) |\psi\rangle \otimes (|0\rangle - |1\rangle) \otimes |1\rangle, \end{aligned} \quad (29)$$

for which we refer to the n -qubit state coupled to the ancillary state $|1\rangle \otimes |0\rangle$ as the success state. By setting the real-time step to Δt_1 defined in Eq. (24), the unnormalized success state from $\mathcal{C}_{\text{filt2}}^{(\tilde{E}_0)}$ is written as (see Appendix E)

$$\sum_k c_k \sin^2 \frac{\pi(E_k - \tilde{E}_0)}{2(\tilde{E}_1 - \tilde{E}_0)} |\phi_k\rangle, \quad (30)$$

where the amplitude of ground state is $\mathcal{O}(\delta E_0^2)$ in contrast to the first-order filtration circuit. The approximate

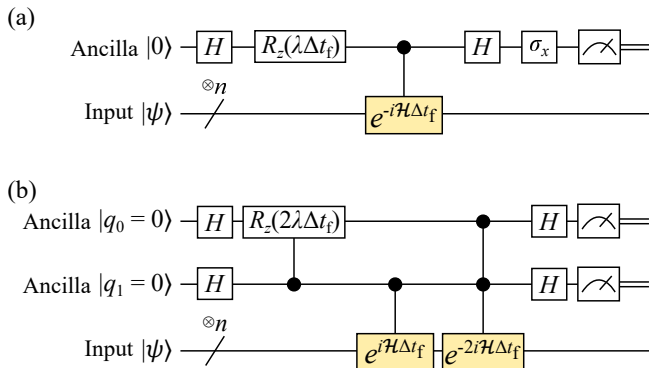


FIG. 6. Circuits (a) $\mathcal{C}_{\text{filt1}}^{(\lambda)}$ for first-order filtration and (b) $\mathcal{C}_{\text{filt2}}^{(\lambda)}$ for second-order filtration specified by a target energy λ . Δt_f is an adjustable real-time step. If λ is equal to one of the energy eigenvalues and the measurement outcome $|0\rangle$ ($|1\rangle \otimes |0\rangle$) for $\mathcal{C}_{\text{filt1}}^{(\lambda)}$ ($\mathcal{C}_{\text{filt2}}^{(\lambda)}$) is obtained, the energy eigenstate belonging to λ has been filtered out from the input state.

upper bound of the allowed total imaginary-time lapse is given by

$$\tau_{\text{ub2}} \approx \frac{1}{E_1 - E_0} \left(\ln \frac{16\varepsilon}{\pi^4} + 2 \ln \left| \frac{c_1}{c_0} \right| + 4 \ln \frac{1}{|\delta E_0|} \right), \quad (31)$$

larger than τ_{ub1} in Eq. (28).

The first- and second-order filtration techniques for the ground state and the first excited state described above are also applicable to other combinations of the energy eigenstates.

III. RESULTS

A. Ground state of an electron in a harmonic potential

Here we perform simulations of PITE for the Fock–Darwin system [41–43], which models the orbital motion of a single electron confined to a plane feeling a harmonic potential and a uniform magnetic field perpendicular to the plane.

1. Setup

We assume that the electron is on the xy plane and, by defining $X \equiv x - L/2$ and $Y \equiv y - L/2$, the potential is given by $V(x, y) = m\omega_0^2(X^2 + Y^2)/2$. Recalling that an electron under a uniform magnetic field in a GaAs quantum dot is often studied (see, e.g., Refs. [44–47]), we adopt the effective electron mass $m = 0.067m_e$, where m_e is the bare electron mass, and the confining strength $\omega_0 = 4$ meV. We set $B = 5$ T for the shifted vector potential $\mathbf{A}(\mathbf{r}) = (x - L/2)B\mathbf{e}_y$ and ignore the spin degree of freedom for simplicity.

We encoded the real-space wave function of the electron by using six qubits for each of the x and y directions. The numerically exact energy eigenstates were obtained by diagonalizing the Hamiltonian matrix in the position representation (see Appendix F). The size $L = 120$ nm of the simulation cell was confirmed to be large enough to get the converged low-energy spectra (see Appendix G 1). The CNOT gate count for the PITE circuit is provided in Appendix H.

2. Ground state from Gaussian initial state

By using the normalized Gaussian wave function

$$g(x, y; x_c, w) \propto \exp\left(-\frac{(X - x_c)^2 + Y^2}{w^2}\right), \quad (32)$$

where x_c specifies the center and w is the width, we defined the initial state $\psi_{\text{init}}(x, y) \equiv g(x, y; 0, 20 \text{ nm})$ centered at the potential bottom. We performed the PITE circuit simulations starting from this initial state for some combinations of the splitting pattern and the amount $\Delta\tau$ of each step. We used $m_0 = 0.9$ in the ITE operator \mathcal{M} for all the simulations. The weight of ground state in the input state at each PITE step for constant- $\Delta\tau$ cases is plotted in the left panel of Fig. 7(a). The total success probability at each step is also plotted. In the cases for $\Delta\tau = 0.02$ meV $^{-1}$, we can see that the weights for the two splitting patterns do not differ much from each other due to the small $\Delta\tau$. Those for $\Delta\tau = 0.05$ meV $^{-1}$, on the other hand, the PITE steps exhibited unstable behavior due to the large step. The oscillatory behavior that may occur when approaching the ground state is a consequence of the approximation using the RTE operators instead of the exact ITE operator (see also Nishi et al. [48]). In addition, the Suzuki-Trotter splitting within each RTE operator can excite the trial state. These two facts make it difficult to find the optimal choice of $\Delta\tau$.

Given the observations above, we performed simulations for a variable imaginary-time step defined in Eq. (1) with $\Delta\tau_{\text{min}} = 0.02$ meV $^{-1}$, $\Delta\tau_{\text{max}} = 0.05$ meV $^{-1}$, and $\kappa = 5$. The results are plotted in the right panel of Fig. 7(a). The TVT splitting gave the better convergence than the TV splitting and the total success probability for the former is higher than that of the latter. In addition, the convergence for the TVT splitting is better than in the constant- $\Delta\tau$ cases shown in the left panel. The reason why the variable- $\Delta\tau$ cases can reach the ground state in contrast to the cases of constant large $\Delta\tau$ is that the high-energy states having significant weights at the early PITE steps are rotated rapidly by a large $\Delta\tau$ in the RTE operator, rendering the approximate ITE inaccurate.

3. Ground state from exponential initial state

Since an efficient way for preparing an exponentially decaying state is known [49], we also performed simula-

tions by using an exponential initial state $\psi_{\text{init}}(x, y) \propto \exp(-(|X| + |Y|)/d)$, where $d = 15$ nm is the decay length. The weight of ground state in the input state at each PITE step for constant- $\Delta\tau$ cases is plotted in the left panel of Fig. 7(b). In the cases for $\Delta\tau = 0.006$ meV $^{-1}$, the convergence is slow for both splitting patterns. For $\Delta\tau = 0.035$ meV $^{-1}$, the convergence is faster. The *TVT* splitting, however, exhibits the slower convergence than the *TV* splitting. The right panel of the figure shows the results for a variable step with $\Delta\tau_{\text{min}} = 0.006$ meV $^{-1}$, $\Delta\tau_{\text{max}} = 0.035$ meV $^{-1}$, and $\kappa = 5$, where the *TVT* splitting gives rise to more rapid convergence than the *TV* splitting. The convergence for the *TVT* splitting is better than in the constant- $\Delta\tau$ cases shown in the left panel, similarly to the cases with the Gaussian initial state.

The results obtained in the simulations above suggest that it is a good choice for adopting the combination of *TVT* splitting and a variable $\Delta\tau$ for achieving rapid convergence for a generic system.

We also simulated the construction of the probability current density, defined as the electric current density divided by $-e$, by using the measurement-based formulae in Eqs. (21) and (22). Figure 7(c) shows the results for the final state obtained for the *TVT* splitting with the variable $\Delta\tau$. The calculated total current density correctly exhibits the counterclockwise motion of the electron around the potential bottom, as understood from the classical picture via the Lorentz force [43, 50].

B. Excited states of an electron in a double-well potential

Here we perform simulations of PITE for an electron confined to a double-well potential that mimics a GaAs double quantum dot adopted by Abolfath et al. [46, 47]

1. Setup

The potential is given by

$$V(x, y) = V_0 \exp\left(-\frac{(X+a)^2 + Y^2}{\Delta^2}\right) + V_0 \exp\left(-\frac{(X-a)^2 + Y^2}{\Delta^2}\right) + V_p \exp\left(-\frac{X^2}{\Delta_x^2} - \frac{Y^2}{\Delta_y^2}\right), \quad (33)$$

where $X \equiv x - L/2$ and $Y \equiv y - L/2$. $V_0 = -59.3$ meV represents the left and right dot potentials. $V_p = 41.51$ meV represents the barrier generated by the plunger gate. $a = 2$ nm specifies the location of left and right dots having widths $\Delta = 24.48$ nm for the symmetric shapes, while the barrier has $\Delta_x = 2.94$ nm and $\Delta_y = 24.48$ nm for the asymmetric shape. We introduce an external magnetic field $B = 3$ T along the z direction for the shifted vector potential and adopt the effective electron mass similarly

to the case of a harmonic potential described above. We ignore the spin degree of freedom for simplicity.

We encoded the real-space wave function of the electron by using six qubits for each of the x and y directions. The size $L = 120$ nm of the simulation cell was confirmed to be large enough to get the converged low-energy spectra (see Appendix G2). We adopted the *TVT* splitting and $m_0 = 0.9$ for all the PITE simulations described below. The CNOT gate count for the PITE circuit is provided in Appendix H.

2. Lowest-energy states within subspaces

Since the target system subject to the magnetic field is invariant under inversion ($X \rightarrow -X$, $Y \rightarrow -Y$), each energy eigenstate has its own positive or negative parity. We found, by looking into the numerically obtained energy eigenstates $|\phi_\nu\rangle$ ($\nu = 0, 1, \dots$), that $|\phi_0\rangle, |\phi_2\rangle, |\phi_5\rangle, |\phi_6\rangle$, and $|\phi_8\rangle$ have positive parity among the lowest ten states, while the other five have negative parity.

To obtain the ground state $|\phi_0\rangle$, we defined the initial state as a bonding s -type orbital

$$\psi_{\text{init}}^{(s+)}(x, y) \propto g(x, y; a, w) + g(x, y; -a, w) \quad (34)$$

with the widths $w = 11$ nm of Gaussian functions, which has positive parity. We performed a PITE circuit simulation starting from this initial guess by using variable imaginary-time step with $\Delta\tau_{\text{min}} = 0.004$ meV $^{-1}$, $\Delta\tau_{\text{max}} = 0.008$ meV $^{-1}$, and $\kappa = 10$. The iterations reached the convergence, as shown in the left panel of Fig. 8(a), where the parity has been correctly preserved throughout the iterations to the final state $|\psi_{\text{fin}}^{(s+)}\rangle$. We also performed a simulation for obtaining the first excited state $|\phi_1\rangle$, which is the lowest-energy state within the negative-parity subspace. We defined the initial state as an anti-bonding s -type orbital

$$\psi_{\text{init}}^{(s-)}(x, y) \propto g(x, y; a, w) - g(x, y; -a, w), \quad (35)$$

which has negative parity. As seen in the results shown in the left panel of Fig. 8(b), the iterations continued by preserving the parity to reach the final state $|\psi_{\text{fin}}^{(s-)}\rangle$.

We calculated the probability current densities of $|\psi_{\text{fin}}^{(s+)}\rangle$ and $|\psi_{\text{fin}}^{(s-)}\rangle$ from the measurement-based formulae, as shown in the right panels of Figs. 8(a) and (b), respectively. In contrast to the opposite parity of the two states, the motions of the electron in them basically coincide with each other. That is, the electron exhibits counterclockwise motion around each potential minimum.

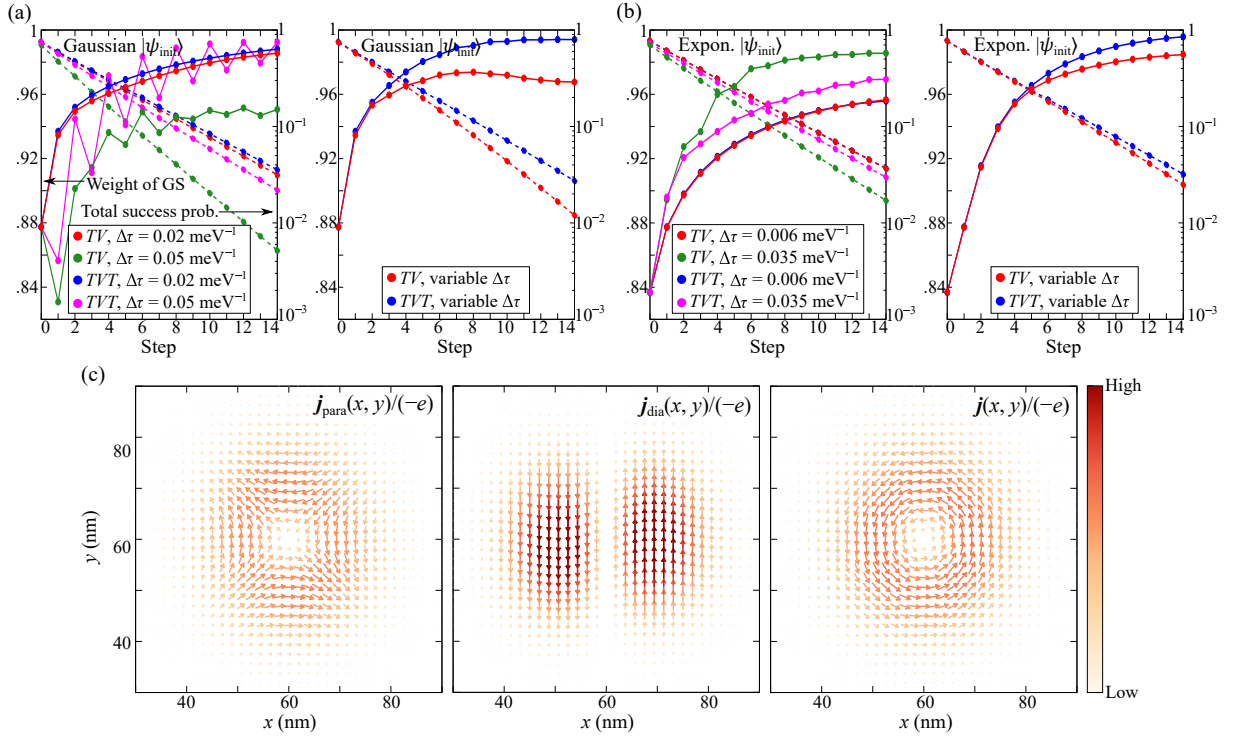


FIG. 7. (a) Circles connected by solid lines in the left panel show the weight of ground state (GS) in the input state at each PITE step with a constant $\Delta\tau$ for a Gaussian initial state. Circles connected by dashed lines in the left panel show the total success probability at each step. The right panel shows similar plots for $\Delta\tau_{\text{min}} = 0.02 \text{ meV}^{-1}$, $\Delta\tau_{\text{max}} = 0.05 \text{ meV}^{-1}$, and $\kappa = 5$. (b) Results for an initial state having an exponential shape. The left panel is for constant- $\Delta\tau$ cases, while the right panel is for $\Delta\tau_{\text{min}} = 0.006 \text{ meV}^{-1}$, $\Delta\tau_{\text{max}} = 0.035 \text{ meV}^{-1}$, and $\kappa = 5$. (c) The paramagnetic, diamagnetic, and total probability current density calculated from the measurement-based formulae for the final state for the *TVT* splitting with the variable $\Delta\tau$.

3. Filtration for obtaining excited states

To obtain the second excited state $|\phi_2\rangle$, we defined the initial state as a σ bonding p_x -type orbital

$$\begin{aligned} \psi_{\text{init}}^{(p_x^+)}(x, y) \propto & g\left(x, y; \frac{3a}{2}, w\right) + g\left(x, y; -\frac{3a}{2}, w\right) \\ & - \frac{5}{2}g(x, y; 0, w), \end{aligned} \quad (36)$$

which has positive parity. We found that this initial guess contains a significant weight 0.45 of $|\phi_2\rangle$ and a non-negligible weight 0.22 of $|\phi_5\rangle$, as inferred from their shapes depicted in the insets of Fig. 9. Therefore, in order for the PITE steps to converge to $|\phi_2\rangle$ rapidly, not only $|\phi_0\rangle$ but also $|\phi_5\rangle$ have to be removed from the initial state. To this end, we applied the first-order filtration circuits $\mathcal{C}_{\text{filt1}}^{(\bar{E}_0)}$ and $\mathcal{C}_{\text{filt1}}^{(\bar{E}_5)}$, described in Sect. II F, for which we assumed the estimated energy eigenvalues of $|\phi_0\rangle$ and $|\phi_2\rangle$ have no error ($\delta E_0 = \delta E_2 = 0$) and that of $|\phi_5\rangle$ can have an error. The results of PITE steps starting from the filtered input state are shown in Fig. 9(a) for three values of the error δE_5 . We used the variable imaginary-time step with $\Delta\tau_{\text{min}} = 0.003 \text{ meV}^{-1}$, $\Delta\tau_{\text{max}} = 0.005 \text{ meV}^{-1}$, and $\kappa = 10$. The results for the input state with

the second-order filtration circuits $\mathcal{C}_{\text{filt2}}^{(\bar{E}_0)}$ and $\mathcal{C}_{\text{filt2}}^{(\bar{E}_5)}$ are also shown in Fig. 9(b). It is seen that the weight of $|\phi_2\rangle$ can decrease slightly after the tenth step despite the monotonic decrease in the weight of $|\phi_5\rangle$. This behavior implies that further application of filtration for removing energy eigenstates other than $|\phi_5\rangle$ on the way to $|\phi_2\rangle$ is needed.

The weights of $|\phi_2\rangle$ and $|\phi_5\rangle$ in the initial state after applying the filtration circuits to $|\psi_{\text{init}}^{(p_x^+)}\rangle$ for removing $|\phi_0\rangle$ and $|\phi_5\rangle$ are plotted in Fig. 10 as functions of the errors δE_2 and δE_5 with $\delta E_0 = 0$. The success probabilities of filtration are also plotted. It is observed that these weights are asymmetric with respect to the signs of δE_2 and δE_5 . The weights of $|\phi_5\rangle$ around $\delta E_5 = 0$ is more suppressed by the second-order filtration than by the first-order one, as expected. The reason for the success probability for the second-order filtration being lower than that for the first-order may be simply that the former distributes the weights in the input to the four possible ancillary states, while the latter does that to the two possible ancillary states.

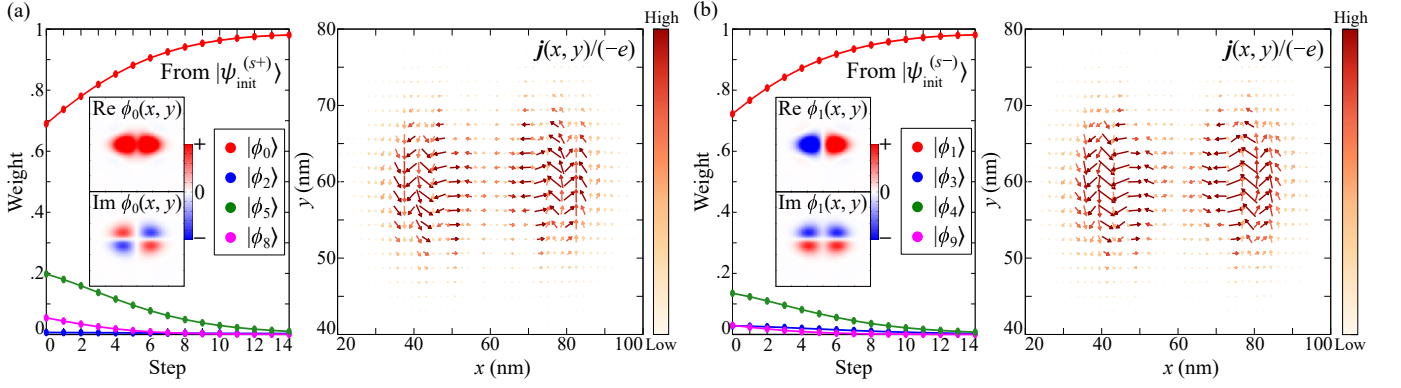


FIG. 8. (a) Left panel shows the weights of the energy eigenstates contained in the input state at each PITE step starting from $|\psi_{init}^{(s+)}\rangle$. The inset draws the ground state in real space. The right panel shows the total probability current density of the final state. (b) Similar plot for $|\psi_{init}^{(s-)}\rangle$. The inset draws the first excited state in real space.

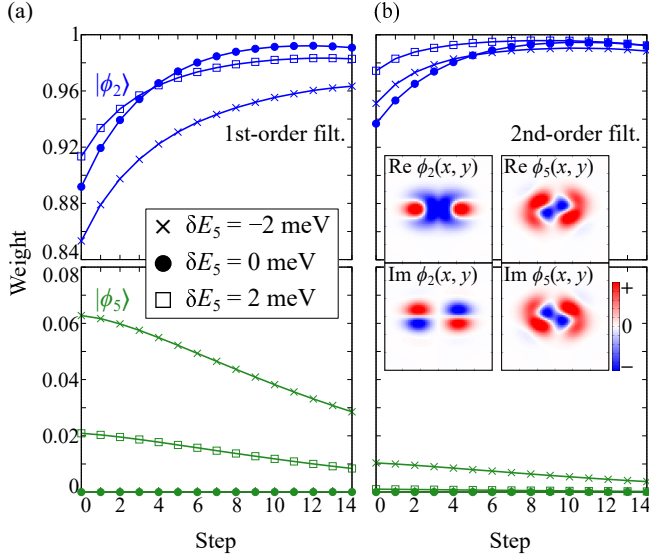


FIG. 9. (a) Weights of $|\phi_2\rangle$ and $|\phi_5\rangle$ in the input state at each PITE step for obtaining $|\phi_2\rangle$. The PITE steps started after applying the first-order filtration circuits with an error δE_5 to $|\psi_{init}^{(p_x+)}\rangle$ for removing $|\phi_0\rangle$ and $|\phi_5\rangle$. (b) Similar plots for the second-order filtration circuits. The inset draws $|\phi_2\rangle$ and $|\phi_5\rangle$ in real space.

IV. CONCLUSIONS

We proposed a method to perform FQE calculation for an electronic system under a uniform magnetic field. The magnetic-phase gate originating from the decoupled evolution operators was found to lead to efficient implementation of the PITE circuit. Resource estimation revealed that introducing a magnetic field into an interacting electronic system does not significantly raise the entire computational cost.

We performed FQE simulations for a confined electron

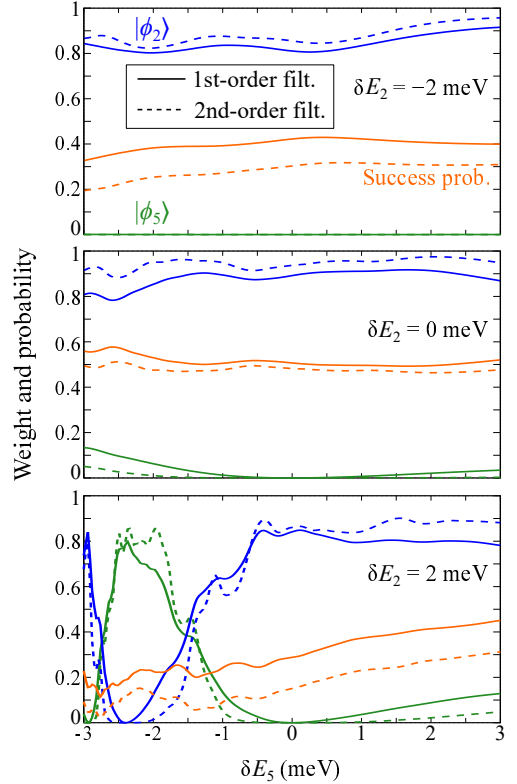


FIG. 10. Weights of $|\phi_2\rangle$ and $|\phi_5\rangle$ in the initial state after applying the filtration circuits to $|\psi_{init}^{(p_x+)}\rangle$ for removing $|\phi_0\rangle$ and $|\phi_5\rangle$ are plotted as functions of the errors δE_2 and δE_5 . The success probabilities of filtration are also plotted.

under a uniform magnetic field, and confirmed that our method correctly provides the ground state, for which the measurement-based formulae for the electric current density was found to work. In addition, the new method in combination with the first- and second-order filtration circuits produced the desired excited states.

The methods proposed in this study allows one to use the FQE framework to obtain the lowest-energy states of a generic molecular or model system subjected to a uniform magnetic field. The techniques for incorporating the magnetic field are also applicable to quantum simulations of real-time dynamics in the first-quantized form. These facts will extend the practical application of quantum computation to analyze static and dynamical properties of interacting electronic systems.

ACKNOWLEDGMENTS

This work was supported by MEXT as ‘‘Program for Promoting Researches on the Supercomputer Fugaku’’ (JPMXP1020200205) and JSPS KAKENHI as ‘‘Grant-in-Aid for Scientific Research(A)’’ Grant Number 21H04553. The computation in this work has been done using (supercomputer Fugaku provided by the RIKEN Center for Computational Science/Supercomputer Center at the Institute for Solid State Physics in the University of Tokyo).

Appendix A: Derivation of Eq. (13)

For each direction, the action of kinetic-phase gate on the computational basis $|j\rangle_n$ ($j = 0, 1, \dots, N-1$) is

$$\begin{aligned} U_{\text{kin}}(\Delta t)|j\rangle_n &= \exp\left(-i\frac{(\tilde{j}\Delta p)^2}{2m}\Delta t\right)|j\rangle_n \\ &= e^{-ie_{\text{kin}}j^2\Delta t}e^{iNe_{\text{kin}}j\Delta t}e^{-iN^2e_{\text{kin}}\Delta t/4}|j\rangle_n. \end{aligned} \quad (\text{A1})$$

By using the binary digits for $j = \sum_{\ell=0}^{n-1} 2^\ell j_\ell$, the contribution from the first-order exponent on the right-hand side of in Eq. (A1) is written as

$$\begin{aligned} e^{iNe_{\text{kin}}j\Delta t}|j\rangle_n &= \prod_{\ell=0}^{n-1} \exp(i2^\ell j_\ell Ne_{\text{kin}}\Delta t)|j\rangle_n \\ &= (Z_{\text{kin}}(2^{n-1}N)|j_{n-1}\rangle) \otimes \dots \otimes (Z_{\text{kin}}(2^1N)|j_1\rangle) \otimes (Z_{\text{kin}}(2^0N)|j_0\rangle) \\ &= \prod_{\ell=0}^{n-1} \overbrace{Z_{\text{kin}}(2^\ell N)}^{\text{On } \ell\text{th qubit}} |j\rangle_n, \end{aligned} \quad (\text{A2})$$

where we introduced the single-qubit phase gate Z_{kin} defined in Eq. (12). The contribution from the second-order exponent is written as

$$\begin{aligned} e^{-ie_{\text{kin}}j^2\Delta t}|j\rangle_n &= \prod_{\ell=0}^{n-1} \prod_{\ell'=0}^{n-1} \exp(-i2^{\ell+\ell'} j_\ell j_{\ell'} e_{\text{kin}}\Delta t)|j\rangle_n \\ &= \left(\prod_{\ell=0}^{n-1} \exp(-i2^{2\ell} j_\ell e_{\text{kin}}\Delta t) \right) \prod_{\ell=0}^{n-1} \prod_{\ell' \neq \ell}^{n-1} \exp(-i2^{\ell+\ell'} j_\ell j_{\ell'} e_{\text{kin}}\Delta t)|j\rangle_n \\ &= (Z_{\text{kin}}(-2^{2n-2}) \otimes \dots \otimes Z_{\text{kin}}(-2^2) \otimes Z_{\text{kin}}(-2^0)) \prod_{\ell=0}^{n-1} \prod_{\ell' \neq \ell}^{n-1} C_{\ell, \ell'} Z_{\text{kin}}(-2^{\ell+\ell'})|j\rangle_n \\ &= (Z_{\text{kin}}(-2^{2n-2}) \otimes \dots \otimes Z_{\text{kin}}(-2^2) \otimes Z_{\text{kin}}(-2^0)) \prod_{\ell=0}^{n-1} \prod_{\ell' < \ell}^{n-1} C_{\ell, \ell'} Z_{\text{kin}}(-2^{\ell+\ell'+1})|j\rangle_n, \end{aligned} \quad (\text{A3})$$

where the two-qubit gate $C_{\ell, \ell'} Z_{\text{kin}}$ acts on the ℓ' th qubit as Z_{kin} controlled by the ℓ th qubit. These gates clearly commutes with each other. We used the relation $C_{\ell, \ell'} Z_{\text{kin}} = C_{\ell', \ell} Z_{\text{kin}}$ to get the last equality in Eq. (A3).

Substitution of Eqs. (A2) and (A3) into Eq. (A1) leads to Eq. (13).

Appendix B: Derivation of Eq. (15)

Let us consider the position eigenstate $|x^{(k)}\rangle \otimes |y^{(k')}\rangle$ specified by the discretized coordinates $x^{(k)} = k\Delta x$ and $y^{(k')} = k'\Delta x$. By using the binary digits for $k = \sum_{\ell=0}^{n-1} 2^\ell k_\ell$ and those for k' similarly, the action of magnetic-phase

gate on the position eigenstate is written as

$$\begin{aligned}
U_{\text{mag}}|x^{(k)}\rangle \otimes |y^{(k')}\rangle &= \exp\left(i\mu x^{(k)}y^{(k')}\right)|x^{(k)}\rangle \otimes |y^{(k')}\rangle \\
&= \exp\left(i\mu\Delta x^2 \sum_{\ell=0}^{n-1} \sum_{\ell'=0}^{n-1} 2^{\ell+\ell'} k_{\ell} k'_{\ell'}\right)|x^{(k)}\rangle \otimes |y^{(k')}\rangle \\
&= \prod_{\ell=0}^{n-1} \prod_{\ell'=0}^{n-1} \exp\left(i2^{\ell+\ell'} k_{\ell} k'_{\ell'} \mu \Delta x^2\right)|x^{(k)}\rangle \otimes |y^{(k')}\rangle \\
&= \prod_{\ell=0}^{n-1} \prod_{\ell'=0}^{n-1} C_{\ell,\ell'} Z_{\text{mag}}^{(\ell+\ell')} |x^{(k)}\rangle \otimes |y^{(k')}\rangle,
\end{aligned} \tag{B1}$$

where we introduced the single-qubit phase gate Z_{mag} defined in Eq. (14). The two-qubit gate $C_{\ell,\ell'} Z_{\text{mag}}^{(\ell+\ell')}$ represents the $Z_{\text{mag}}^{(\ell+\ell')}$ gate on the ℓ' th qubit for the y position coordinate controlled by the ℓ th qubit for the x position coordinate. From the fact that these gates commute with each other and Eq. (B1), it is now clear that U_{mag} can be written as Eq. (15).

Appendix C: Calculation of derivative distributions via repeated measurements

Here we consider a differentiable complex function f of m continuous real variables x_0, \dots, x_{m-1} . We denote them by \mathbf{x} collectively. We assume that we do not know the functional form of f . For a given r , we want to calculate the distributions

$$g_{r_0, r_1, \dots, r_{m-1}}^{(r_0+r_1+\dots+r_{m-1})}(\mathbf{x}) \equiv f(\mathbf{x}) \frac{1}{r_0! r_1! \dots r_{m-1}!} \frac{\partial^{r_0+r_1+\dots+r_{m-1}} f(\mathbf{x})^*}{\partial x_0^{r_0} \partial x_1^{r_1} \dots \partial x_{m-1}^{r_{m-1}}}, \tag{C1}$$

which we call the derivative distributions, as functions of \mathbf{x} for all the possible combinations (r_0, \dots, r_{m-1}) satisfying $r_0 + \dots + r_{m-1} \leq r$. We describe below a generic procedure for calculating them via repeated measurements for qubits which encode f .

1. Linear equations based on finite differences

By performing the multivariate Taylor expansion of f around a point \mathbf{x} , we can write

$$f(\mathbf{x} + \mathbf{h}) = \sum_{\ell=0}^{\infty} \sum_{r_0+\dots+r_{m-1}=\ell} \frac{1}{r_0! \dots r_{m-1}!} \frac{\partial^{\ell} f(\mathbf{x})}{\partial x_0^{r_0} \dots \partial x_{m-1}^{r_{m-1}}} h_0^{r_0} \dots h_{m-1}^{r_{m-1}} \tag{C2}$$

for an arbitrary m -dimensional vector \mathbf{h} . This expression and Eq. (C1) lead to

$$f(\mathbf{x}) f(\mathbf{x} + \mathbf{h})^* = \sum_{\ell=0}^{\infty} \sum_{(r_0, \dots, r_{m-1}) \in \mathcal{D}(\ell)} g_{r_0, \dots, r_{m-1}}^{(\ell)}(\mathbf{x}) h_0^{r_0} \dots h_{m-1}^{r_{m-1}}, \tag{C3}$$

where $\mathcal{D}(\ell)$ is the set of the combinations (r_0, \dots, r_{m-1}) of nonnegative integers that satisfy $r_0 + \dots + r_{m-1} = \ell$ for the ℓ th-order derivatives. We can easily understand that the number of elements in $\mathcal{D}(\ell)$ is given by

$$|\mathcal{D}(\ell)| = \frac{(\ell + m - 1)!}{\ell!(m - 1)!}. \tag{C4}$$

We can see Eq. (C3) as a linear equation for an infinite number of unknown distributions $g_{r_0, \dots, r_{m-1}}^{(\ell)}$. To eliminate the contributions on the order of h^{r+1} , we define

$$G^{(r)}(\mathbf{x}, \mathbf{h}) \equiv \frac{f(\mathbf{x}) f(\mathbf{x} + \mathbf{h})^* + (-1)^r f(\mathbf{x}) f(\mathbf{x} - \mathbf{h})^*}{2} \tag{C5}$$

for an integer r . Substituting Eq. (C2) into this definition, we obtain

$$G^{(r)}(\mathbf{x}, \mathbf{h}) = \begin{cases} \sum_{\text{even } \ell}^r \sum_{(r_0, \dots, r_{m-1}) \in \mathcal{D}(\ell)} g_{r_0, \dots, r_{m-1}}^{(\ell)}(\mathbf{x}) h_0^{r_0} \cdots h_{m-1}^{r_{m-1}} + \mathcal{O}(h^{r+2}) & \text{even } r \\ \sum_{\text{odd } \ell}^r \sum_{(r_0, \dots, r_{m-1}) \in \mathcal{D}(\ell)} g_{r_0, \dots, r_{m-1}}^{(\ell)}(\mathbf{x}) h_0^{r_0} \cdots h_{m-1}^{r_{m-1}} + \mathcal{O}(h^{r+2}) & \text{odd } r \end{cases}. \quad (\text{C6})$$

We omit the terms whose orders are higher than h^r in this expression to construct a linear equation for the finite number of unknowns. The number of unknowns is given by

$$N^{(r)} = \begin{cases} \sum_{\text{even } \ell}^r |\mathcal{D}(\ell)| & \text{even } r \\ \sum_{\text{odd } \ell}^r |\mathcal{D}(\ell)| & \text{odd } r \end{cases}. \quad (\text{C7})$$

The linear equation for an even (odd) r provides an approximate solution with an error on the order of h^{r+2} (h^{r+1}). We need $N^{(r)}$ independent conditions for solving the linear equation. In practice, we adopt some small vectors \mathbf{h}_d ($d = 0, \dots, N^{(r)} - 1$) and calculate $G^{(r)}(\mathbf{x}, \mathbf{h}_d)$ via the definition in Eq. (C5) to construct the linear equation in Eq. (C6) to be solved on a classical computer.

2. Circuits for calculation of $G^{(r)}$

If a many-qubit system which encodes f is available, it is possible to obtain the derivative distributions by using the circuits explained below.

We assume that we have n qubits for each of the m variables and assign each computational basis $|j\rangle_n$ ($j = 0, \dots, 2^n - 1$) to equidistant grid points on a range $[0, L]$: $x^{(j)} = j\Delta x$, where $\Delta x \equiv L/N$. We assume further that the unknown function f is available as a normalized mn -qubit state

$$|f\rangle = \sum_{j_0, \dots, j_{m-1}}^{N-1} f(x^{(j_0)}, \dots, x^{(j_{m-1})}) |j_0\rangle_n \otimes \cdots \otimes |j_{m-1}\rangle_n, \quad (\text{C8})$$

where $N \equiv 2^n$. The probability for finding $|\mathbf{x}\rangle$ in an mn -qubit measurement on $|f\rangle$ is $\mathbb{P}_{\mathbf{x}} = |f(\mathbf{x})|^2$. We want to obtain the derivative distributions, defined in Eq. (C1), at the grid points. To this end, we have to calculate $G^{(r)}(\mathbf{x}, \mathbf{h})$ for an arbitrary displacement vector \mathbf{h} for constructing the linear equation.

From an n -qubit phase gate $U_{\text{shift}}(d)$ for an integer d defined via $|j\rangle_n \mapsto \exp(-i2\pi dj/N) |j\rangle_n$ ($j = 0, \dots, N-1$), we define

$$\mathcal{U}(d) \equiv \text{QFT} \cdot U_{\text{shift}}(d) \cdot \text{QFT}^\dagger. \quad (\text{C9})$$

When this operator acts on the n qubits responsible for the variable x_0 , it displaces the function f by $d\Delta x$ in the x_0 direction as follows:

$$\begin{aligned} |f\rangle &\xrightarrow{\text{QFT}^\dagger} \sum_{j_0, \dots, j_{m-1}}^{N-1} f(j_0\Delta x, j_1\Delta x, \dots) \frac{1}{\sqrt{N}} \sum_{k_0=0}^{N-1} \exp\left(\frac{-2\pi i j_0 k_0}{N}\right) |k_0\rangle_n \otimes |j_1\rangle_n \otimes \cdots \otimes |j_{m-1}\rangle_n \\ &\xrightarrow{U_{\text{shift}}(d)} \sum_{j_0, \dots, j_{m-1}}^{N-1} f(j_0\Delta x, j_1\Delta x, \dots) \frac{1}{\sqrt{N}} \sum_{k_0=0}^{N-1} \exp\left(\frac{2\pi i (-j_0 - d) k_0}{N}\right) |k_0\rangle_n \otimes |j_1\rangle_n \otimes \cdots \otimes |j_{m-1}\rangle_n \\ &\xrightarrow{\text{QFT}} \sum_{j_0, \dots, j_{m-1}}^{N-1} f(j_0\Delta x, j_1\Delta x, \dots) \frac{1}{N} \sum_{k_0, k'_0=0}^{N-1} \exp\left(\frac{2\pi i (-j_0 - d + k'_0) k_0}{N}\right) |k'_0\rangle_n \otimes |j_1\rangle_n \otimes \cdots \otimes |j_{m-1}\rangle_n \\ &= \sum_{j_0, \dots, j_{m-1}}^{N-1} f(j_0\Delta x, j_1\Delta x, \dots) |j_0 + d \bmod N\rangle_n \otimes |j_1\rangle_n \otimes \cdots \otimes |j_{m-1}\rangle_n \\ &= |f \text{ shifted by } d\Delta x \text{ in } x_0\rangle. \end{aligned} \quad (\text{C10})$$

This is also the case for the other variables.

For a vector \mathbf{d} specified by m integers, we introduce the circuit $\mathcal{C}^{(\phi)}[\mathbf{d}]$ with an angle parameter ϕ , as shown in Fig. 11. The state of input $(mn+1)$ -qubit system consisting of the encoded function and the ancilla changes until the measurement as

$$|f\rangle \otimes \overbrace{|0\rangle}^{\text{Ancilla}} \mapsto \frac{|f\rangle + e^{i\phi}|f[\mathbf{d}]\rangle}{2} \otimes |0\rangle + \frac{|f\rangle - e^{i\phi}|f[\mathbf{d}]\rangle}{2} \otimes |1\rangle \equiv |\Psi[\mathbf{d}]\rangle, \quad (\text{C11})$$

where $|f[\mathbf{d}]\rangle$ represents f displaced by $\mathbf{h} \equiv \mathbf{d}\Delta x$. The measurement is described by the $2N^m$ projection operators

$$\mathcal{P}_{xq} \equiv |\mathbf{x}\rangle\langle\mathbf{x}| \otimes |q\rangle\langle q| \quad (x_0, \dots, x_{m-1} = 0, \Delta x, \dots, (N-1)\Delta x, q = 0, 1). \quad (\text{C12})$$

The probability for obtaining $|\mathbf{x}\rangle \otimes |0\rangle$ as the outcome of measurement is thus, from Eq. (C11),

$$\begin{aligned} \mathbb{P}_{x0}(\mathbf{d}) &= \|\mathcal{P}_{x0}|\Psi[\mathbf{d}]\rangle\|^2 \\ &= \frac{|f(\mathbf{x})|^2 + |f(\mathbf{x} - \mathbf{h})|^2}{4} + \frac{\cos \phi}{2} \text{Re}(f(\mathbf{x})f(\mathbf{x} - \mathbf{h})^*) + \frac{\sin \phi}{2} \text{Im}(f(\mathbf{x})f(\mathbf{x} - \mathbf{h})^*) \end{aligned} \quad (\text{C13})$$

This expression means that we can obtain the relation which connects the probability for $\phi = 0$ ($\phi = \pi/2$) and the real (the imaginary) part of $f(\mathbf{x})f(\mathbf{x} - \mathbf{h})^*$:

$$f(\mathbf{x})f(\mathbf{x} - \mathbf{h})^* = 2 \left(\mathbb{P}_{x0}^{(\text{real})}(\mathbf{d}) + i\mathbb{P}_{x0}^{(\text{imag})}(\mathbf{d}) \right) - (\mathbb{P}_x + \mathbb{P}_{x-\mathbf{h}}) \frac{1+i}{2}. \quad (\text{C14})$$

The definition in Eq. (C5) of the desired quantity allows us to calculate it only from the probabilities as

$$G^{(r)}(\mathbf{x}, \mathbf{h}) = \begin{cases} \mathbb{P}_{x0}^{(\text{real})}(-\mathbf{d}) + i\mathbb{P}_{x0}^{(\text{imag})}(-\mathbf{d}) + \mathbb{P}_{x0}^{(\text{real})}(\mathbf{d}) + i\mathbb{P}_{x0}^{(\text{imag})}(\mathbf{d}) - \frac{1+i}{4}(2\mathbb{P}_x + \mathbb{P}_{x+\mathbf{h}} + \mathbb{P}_{x-\mathbf{h}}) & \text{even } r \\ \mathbb{P}_{x0}^{(\text{real})}(-\mathbf{d}) + i\mathbb{P}_{x0}^{(\text{imag})}(-\mathbf{d}) - \mathbb{P}_{x0}^{(\text{real})}(\mathbf{d}) - i\mathbb{P}_{x0}^{(\text{imag})}(\mathbf{d}) - \frac{1+i}{4}(\mathbb{P}_{x+\mathbf{h}} - \mathbb{P}_{x-\mathbf{h}}) & \text{odd } r \end{cases}. \quad (\text{C15})$$

In short, we can obtain the derivative distributions by solving the linear equation in Eq. (C6) on a classical computer by collecting data of $G^{(r)}$ for various \mathbf{d} vectors from repeated measurements on a quantum computer. It should be stressed here that this method does not involve the complex value of f itself. (In fact, we cannot know the shape of this complex function from this method.) This characteristics of the method is favorable from a practical viewpoint since the prepared $|f\rangle$ state for each measurement is not guaranteed to have a global phase common to all the measurements.

3. An example for $m = 2$

Let us consider a case where f is a two-variable function ($m = 2$). Eqs. (C4) and (C7) give $N^{(1)} = 2$ for the first-order derivative distributions. If we adopt, for example, two displacement vectors $\mathbf{h}_0 \equiv \mathbf{e}_0\Delta x$ and $\mathbf{h}_1 \equiv \mathbf{e}_1\Delta x$ (\mathbf{e}_0 and \mathbf{e}_1 are the unit vector in the x_0 and x_1 directions, respectively), the linear equation is constructed from Eq. (C6) as

$$\begin{pmatrix} G^{(1)}(\mathbf{x}, \mathbf{h}_0) \\ G^{(1)}(\mathbf{x}, \mathbf{h}_1) \end{pmatrix} = \begin{pmatrix} \Delta x & 0 \\ 0 & \Delta x \end{pmatrix} \begin{pmatrix} g_{1,0}^{(1)}(\mathbf{x}) \\ g_{0,1}^{(1)}(\mathbf{x}) \end{pmatrix}. \quad (\text{C16})$$

For the second-order distributions, on the other hand, we have $N^{(2)} = 4$. If we adopt, for example, four displacement vectors $\mathbf{h}'_0 \equiv \mathbf{e}_0\Delta x$, $\mathbf{h}'_1 \equiv \mathbf{e}_1\Delta x$, $\mathbf{h}'_2 \equiv (\mathbf{e}_0 + \mathbf{e}_1)\Delta x$, $\mathbf{h}'_3 \equiv (\mathbf{e}_0 - \mathbf{e}_1)\Delta x$, the linear equation to be solved is constructed as

$$\begin{pmatrix} G^{(2)}(\mathbf{x}, \mathbf{h}'_0) \\ G^{(2)}(\mathbf{x}, \mathbf{h}'_1) \\ G^{(2)}(\mathbf{x}, \mathbf{h}'_2) \\ G^{(2)}(\mathbf{x}, \mathbf{h}'_3) \end{pmatrix} = \begin{pmatrix} 1 & \Delta x^2 & 0 & 0 \\ 1 & 0 & 0 & \Delta x^2 \\ 1 & \Delta x^2 & \Delta x^2 & \Delta x^2 \\ 1 & \Delta x^2 & -\Delta x^2 & \Delta x^2 \end{pmatrix} \begin{pmatrix} g_{0,0}^{(2)}(\mathbf{x}) \\ g_{2,0}^{(2)}(\mathbf{x}) \\ g_{1,1}^{(2)}(\mathbf{x}) \\ g_{0,2}^{(2)}(\mathbf{x}) \end{pmatrix}. \quad (\text{C17})$$

Appendix D: Derivation of Eq. (22)

We can assume that the index of the single electron on which the circuit $\mathcal{C}_{\text{para},x}(d)$ in Fig. 5 acts is 0 without loss of generality.

The paramagnetic current density $j_{\text{para},x}$ can be seen as a special case of the derivative distribution already explained in Appendix C for $3n_e$ variables and $r = 1$. Specifically, from Eq. (19), the unknown distribution in this case is

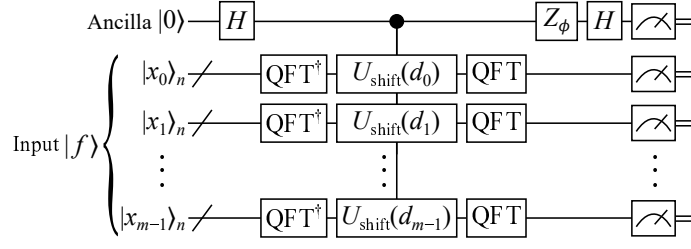


FIG. 11. $(mn + 1)$ -qubit circuit $\mathcal{C}^{(\phi)}[\mathbf{d}]$ for obtaining the real or imaginary part of $f(\mathbf{x})f(\mathbf{x} - \mathbf{h})^*$. $Z_\phi \equiv |0\rangle\langle 0| + e^{i\phi}|1\rangle\langle 1|$ is a single-qubit phase gate. $\mathcal{C}^{(\phi=0)}[\mathbf{d}]$ is used for obtaining the real part, while $\mathcal{C}^{(\phi=\pi/2)}[\mathbf{d}]$ is for the imaginary part.

$\text{Im}\partial\gamma(\mathbf{r}, \mathbf{r}')/\partial x|_{\mathbf{r}'=\mathbf{r}} = -\text{Im}\partial\gamma(\mathbf{r}', \mathbf{r})/\partial x|_{\mathbf{r}'=\mathbf{r}}$. That has the relation to the many-electron wave function Ψ as [see Eq. (17)]

$$\frac{\partial\gamma(\mathbf{r}', \mathbf{r})}{\partial x} \propto \int d^3\mathbf{r}_1 \cdots d^3\mathbf{r}_{n_e-1} \Psi(\mathbf{r}', \mathbf{r}_1, \dots, \mathbf{r}_{n_e-1}) \frac{\partial\Psi(\mathbf{r}, \mathbf{r}_1, \dots, \mathbf{r}_{n_e-1})^*}{\partial x}, \quad (\text{D1})$$

meaning that Ψ corresponds to f in Eq. (C1). The circuit $\mathcal{C}^{(\phi=\pi/2)}[\mathbf{d}]$ in Fig. 11 with a displacement vector $\mathbf{d} = \mathbf{e}_{0x}d\Delta x$ (\mathbf{e}_{0x} is a $3n_e$ -dimensional unit vector along the x direction for the 0th electron) is almost equivalent to $\mathcal{C}_{\text{para},x}(d)$ in Fig. 5. These two circuits differ only in that the $3n(n_e - 1)$ qubits for electrons are not measured in $\mathcal{C}_{\text{para},x}(d)$, while all the $3nn_e$ qubits are measured in $\mathcal{C}^{(\phi=\pi/2)}[\mathbf{d}]$. This difference is correctly taken into account for the RHS of Eq. (C15) by tracing out the degrees of freedom of the unobserved $n_e - 1$ electrons as

$$\begin{aligned} & \sum_{\mathbf{x}_1, \dots, \mathbf{x}_{n_e-1}} \left(\mathbb{P}_{\mathbf{x}_0}^{(\text{imag})}(-\mathbf{d}) - \mathbb{P}_{\mathbf{x}_0}^{(\text{imag})}(\mathbf{d}) - \frac{1}{4}(\mathbb{P}_{\mathbf{x}+\mathbf{h}} - \mathbb{P}_{\mathbf{x}-\mathbf{h}}) \right) \\ &= \mathbb{P}_{\mathbf{x}_0 0}(-d) - \mathbb{P}_{\mathbf{x}_0 0}(d) - \frac{\Delta V}{4n_e} (\rho(\mathbf{x}_0 + d\Delta x \mathbf{e}_x) - \rho(\mathbf{x}_0 - d\Delta x \mathbf{e}_x)), \end{aligned} \quad (\text{D2})$$

where $\mathbb{P}_{\mathbf{x}_0 0}(\pm d)$ are the probabilities in terms of $\mathcal{C}_{\text{para},x}(\pm d)$. Since the quantity in the expression above constitutes the linear equation for $\text{Im}\partial\gamma(\mathbf{r}', \mathbf{r})/\partial x|_{\mathbf{r}'=\mathbf{r}}$, we get to Eq. (22) for $j_{\text{para},x}$.

Appendix E: Derivation of Eqs. (25) and (30)

1. For first-order filtration

We expand the input state in terms of the energy eigenstates as $|\psi\rangle = \sum_k c_k |\phi_k\rangle$ for the filtration circuit $\mathcal{C}_{\text{filt}1}^{(\tilde{E}_0)}$. Substitution of this into the $(n + 1)$ -qubit state in Eq. (23) for an arbitrary real-time step Δt_f leads to

$$\begin{aligned} & \sum_k c_k \left(\frac{e^{-i\tilde{E}_0\Delta t_f/2} - e^{i(\tilde{E}_0/2 - E_k)\Delta t_f}}{2} |\phi_k\rangle \otimes |0\rangle + \frac{e^{-i\tilde{E}_0\Delta t_f/2} + e^{i(\tilde{E}_0/2 - E_k)\Delta t_f}}{2} |\phi_k\rangle \otimes |1\rangle \right) \\ &= \sum_k c_k e^{-iE_k\Delta t_f/2} \left(i \sin \frac{(E_k - \tilde{E}_0)\Delta t_f}{2} |\phi_k\rangle \otimes |0\rangle + \cos \frac{(E_k - \tilde{E}_0)\Delta t_f}{2} |\phi_k\rangle \otimes |1\rangle \right). \end{aligned} \quad (\text{E1})$$

As we set Δt_f to Δt_1 , defined in Eq. (24), the unnormalized success state in the equation above is written as

$$c_0 \exp \left(-i \frac{\pi E_0}{2(\tilde{E}_1 - \tilde{E}_0)} \right) \sin \frac{\pi \delta E_0}{2(\tilde{E}_1 - \tilde{E}_0)} |\phi_0\rangle + \sum_{k \neq 0} c_k \exp \left(-i \frac{\pi E_k}{2(\tilde{E}_1 - \tilde{E}_0)} \right) \sin \frac{\pi(E_k - \tilde{E}_0)}{2(\tilde{E}_1 - \tilde{E}_0)} |\phi_k\rangle, \quad (\text{E2})$$

where the amplitude of ground state is clearly $\mathcal{O}(\delta E_0)$. If the estimated energy eigenvalues of the ground and the first-excited states have no errors ($\delta E_0 = \delta E_1 = 0$), the weight of $|\phi_1\rangle$ in the equation above is $|c_k|^2 \sin^2(\pi/2) = |c_k|^2$, achieving the maximum of \sin^2 factor, which explains the appropriateness of Δt_1 .

2. For second-order filtration

We substitute the input state $|\psi\rangle$ expanded in terms of the energy eigenstate for the filtration circuit $\mathcal{C}_{\text{filt2}}^{(\tilde{E}_0)}$ into Eq. (29) for an arbitrary Δt_f to get the unnormalized success state

$$\sum_k c_k \sin^2 \frac{(E_k - \tilde{E}_0)\Delta t_f}{2} |\phi_k\rangle. \quad (\text{E3})$$

As we set Δt_f to Δt_1 , this state is written as

$$c_0 \sin^2 \frac{\pi\delta E_0}{2(\tilde{E}_1 - \tilde{E}_0)} |\phi_0\rangle + \sum_{k \neq 0} c_k \sin^2 \frac{\pi(E_k - \tilde{E}_0)}{2(\tilde{E}_1 - \tilde{E}_0)} |\phi_k\rangle, \quad (\text{E4})$$

where the amplitude of ground state is clearly $\mathcal{O}(\delta E_0^2)$. If the estimated energy eigenvalues of the ground and the first-excited states have no errors, the weight of $|\phi_1\rangle$ in the equation above achieves the maximum as well as in the first-order filtration.

Appendix F: Matrix elements of a single-particle Hamiltonian

Here we provide the expression of matrix elements of a generic single-particle Hamiltonian.

The matrix element of the kinetic-energy operator in Eq. (5), or equivalently the kinetic propagator, between the position eigenstates $|\mathbf{r}^{(\mathbf{k})}\rangle$ and $|\mathbf{r}^{(\mathbf{k}')}\rangle$ is calculated as

$$\begin{aligned} \langle \mathbf{r}^{(\mathbf{k})} | \hat{T} | \mathbf{r}^{(\mathbf{k}')}\rangle &= \frac{1}{2m} \langle \mathbf{r}^{(\mathbf{k})} | \left(\hat{\mathbf{p}} - \frac{q}{c} \mathbf{A}(\mathbf{r}^{(\mathbf{k})}) \right) \cdot \left(\hat{\mathbf{p}} - \frac{q}{c} \mathbf{A}(\mathbf{r}^{(\mathbf{k}')}) \right) | \mathbf{r}^{(\mathbf{k}')}\rangle \\ &= \frac{1}{2m} \langle \mathbf{r}^{(\mathbf{k})} | \left(\hat{\mathbf{p}} - \frac{q}{c} \mathbf{A}(\mathbf{r}^{(\mathbf{k})}) \right) \cdot \left(\hat{\mathbf{p}} - \frac{q}{c} \mathbf{A}(\mathbf{r}^{(\mathbf{k}')}) \right) \left(\sum_{s_x, s_y, s_z=0}^{N-1} |\mathbf{p}^{(\tilde{\mathbf{s}})}\rangle \langle \mathbf{p}^{(\tilde{\mathbf{s}})}| \right) | \mathbf{r}^{(\mathbf{k}')}\rangle \\ &= \frac{1}{N^3} \sum_{s_x, s_y, s_z=0}^{N-1} \frac{1}{2m} \left(\mathbf{p}^{(\tilde{\mathbf{s}})} - \frac{q}{c} \mathbf{A}(\mathbf{r}^{(\mathbf{k})}) \right) \cdot \left(\mathbf{p}^{(\tilde{\mathbf{s}})} - \frac{q}{c} \mathbf{A}(\mathbf{r}^{(\mathbf{k}')}) \right) \exp \left(i\mathbf{p}^{(\tilde{\mathbf{s}})} \cdot \left(\mathbf{r}^{(\mathbf{k})} - \mathbf{r}^{(\mathbf{k}')}\right) \right) \\ &= \frac{1}{N^3} \sum_{s_x, s_y, s_z=0}^{N-1} \sum_{\nu=x,y,z} \frac{1}{2m} \Pi_{\nu \mathbf{k} \mathbf{s}} \Pi_{\nu \mathbf{k}' \mathbf{s}}^*, \end{aligned} \quad (\text{F1})$$

where the second equality was obtained by employing the fact that the momentum eigenstates in Eq. (3) form a complete orthonormal system for $3n$ -qubit states. Π_{ν} is a N^3 -dimensional non-hermitian matrix. Its (\mathbf{k}, \mathbf{s}) component is defined as

$$\Pi_{\nu \mathbf{k} \mathbf{s}} \equiv \left(p_{\nu}^{(\tilde{\mathbf{s}})} - \frac{q}{c} A_{\nu}(\mathbf{r}^{(\mathbf{k})}) \right) \exp \left(i\mathbf{p}^{(\tilde{\mathbf{s}})} \cdot \mathbf{r}^{(\mathbf{k})} \right). \quad (\text{F2})$$

The matrix element of the potential operator is given by

$$\langle \mathbf{r}^{(\mathbf{k})} | \hat{V} | \mathbf{r}^{(\mathbf{k}')}\rangle = V(\mathbf{r}^{(\mathbf{k})}) \delta_{\mathbf{k} \mathbf{k}'}. \quad (\text{F3})$$

Appendix G: Energy spectra

1. For the harmonic potential in Sect. III A

The lowest ten energy eigenvalues of the Fock–Darwin system obtained by numerical diagonalization for the simulation cell size $L = 120$ nm for 12 qubits (six for each of x and y directions) are shown as circles in Fig. 12 as functions of the external magnetic field B . By using the cyclotron frequency $\omega_c \equiv \sqrt{|eB|/(mc)}$ of the electron, having

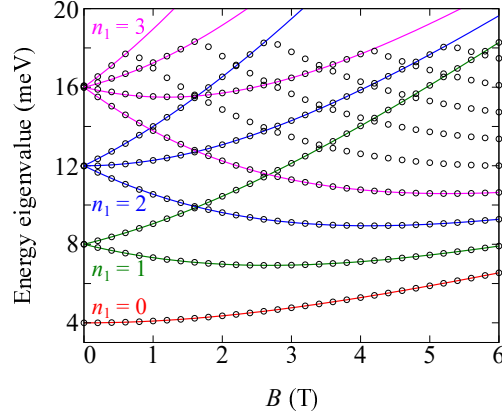


FIG. 12. Circles represent the lowest ten energy eigenvalues of the Fock–Darwin system for each of B obtained by numerical diagonalization of the Hamiltonian. Solid curves represent those obtained by the analytic expression in Eq. (G1), specified by quantum numbers n_1 and ℓ .

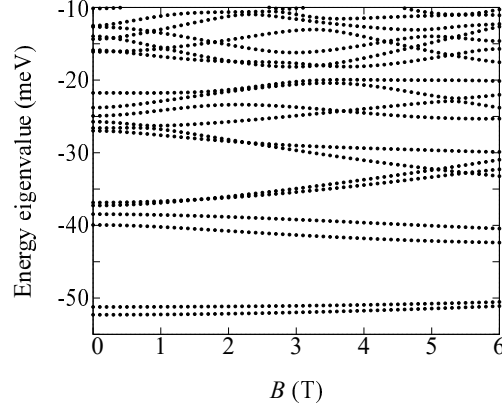


FIG. 13. Circles represent the single-electron energy spectra for the double-well potential for each of B obtained by numerical diagonalization of the Hamiltonian.

the charge e , and $\Omega \equiv \sqrt{\omega_0^2 + \omega_c^2/4}$, the analytic expression for the energy eigenvalues is known to be given by two quantum numbers as $E_{n_1\ell} = (n_1 + 1)\Omega - \ell\omega_c/2$ for $n_1 = 0, 1, \dots$ and

$$\ell = \begin{cases} 0, \pm 2, \pm 4, \dots, \pm n_1 & \text{for even } n_1 \\ \pm 1, \pm 3, \dots, \pm n_1 & \text{for odd } n_1 \end{cases}. \quad (\text{G1})$$

The analytically obtained eigenvalues for $n_1 \leq 3$ are also shown as the solid curves in the figure.

2. For the double-well potential in Sect. III B

The lowest energy eigenvalues of an electron for the double-well potential in Eq. (33) obtained by numerical diagonalization are shown as circles in Fig. 13 as functions of the external magnetic field B . The simulation cell size $L = 120$ nm for 12 qubits (six for each of x and y directions) was used.

Appendix H: CNOT gate counts for the PITE circuits in the simulations

Here we consider the CNOT gate counts for the PITE circuits used in our simulations. They are good measures of the computational cost since it is well known that two-qubit gates are in general much prone to errors and spend

much longer time than single-qubit gates on a real quantum computer.

1. Expressions for generic potentials

Since the simulations are for a single electron in two-dimensional space, the number of CNOT gates in a single PITE step using the TV splitting is calculated as

$$c^{(TV)} = c(U_{\text{pot}}) + c(CU_{\text{pot}}) + 6c(\text{QFT}) + 2c(U_{\text{kin}}) + 2c(CU_{\text{kin}}) + 2c(U_{\text{mag}}), \quad (\text{H1})$$

where we used the fact that each phase gate and its squared form have the same circuit structure (see also Fig. 4). From Figs. 1(c) and 2(a), that for the TVT splitting is similarly calculated as

$$c^{(TVT)} = c(U_{\text{pot}}) + c(CU_{\text{pot}}) + 14c(\text{QFT}) + 4c(U_{\text{kin}}) + 4c(CU_{\text{kin}}) + 6c(U_{\text{mag}}). \quad (\text{H2})$$

Recalling that any singly-controlled single-qubit operation can be implemented by using two CNOT gates [29, 51], we find that the ordinary implementation of QFT [29] involves $c(\text{QFT}) = n^2 + n/2$ CNOT gates for $n = 6$ in our simulations. From Eq. (15), the gate count for the magnetic-phase gate is $c(U_{\text{mag}}) = 2n^2$.

From Eq. (13), U_{kin} contains $n(n-1)/2$ controlled phase gates. Its gate count is thus $c(U_{\text{kin}}) = n(n-1)$. The controlled kinetic-phase gate consists of n singly controlled single-qubit gates and $c(U_{\text{kin}})$ doubly controlled single-qubit gates. It is known that any doubly controlled single-qubit gate can be implemented by using six CNOT gates [29, 51]. Thus we have $c(CU_{\text{kin}}) = 3n^2 - n$.

Gathering the observations above, we can rewrite Eqs. (H1) and (H2) as

$$c^{(TV)} = c(U_{\text{pot}}) + c(CU_{\text{pot}}) + 18n^2 - 2n \quad (\text{H3})$$

and

$$c^{(TVT)} = c(U_{\text{pot}}) + c(CU_{\text{pot}}) + 42n^2 - n, \quad (\text{H4})$$

respectively.

2. For the harmonic potential in Sect. III A

The potential-evolution operator in this case is factorized as $U_{\text{pot}}(\Delta t) = \exp(-im\omega_0^2(x-L/2)^2\Delta t/2) \exp(-im\omega_0^2(y-L/2)^2\Delta t/2)$. Each of the two operators on the right-hand side has a similar functional form to $U_{\text{kin}}(\Delta t)$ [see Eq. (A1)]. Thus we have the gate counts $c(U_{\text{pot}}) = 2c(U_{\text{kin}})$ and $c(CU_{\text{pot}}) = 2c(CU_{\text{kin}})$. From Eqs. (H3) and (H4), the gate counts for the entire PITE step are calculated as $c^{(TV)} = 26n^2 - 5n = 906$ and $c^{(TVT)} = 50n^2 - 5n = 1770$.

3. For the double-well potential in Sect. III B

There can be various implementation of the potential-evolution operator in this case. We adopt here one possible implementation for which we consider the gate counts. We introduce an n_a -qubit auxiliary register to define the squared-distance unitary via

$$S(x_c, d_x) \left(|x^{(k)}\rangle \otimes |0\rangle_{n_a} \right) = |x^{(k)}\rangle \otimes \left| \frac{(x^{(k)} - x_c)^2}{d_x^2} \right\rangle_{n_a} \quad (\text{H5})$$

for each k and k' , where the center x_c and the width d_x are predetermined circuit parameters. The state of the auxiliary register on the right-hand side of Eq. (H5) is one of the states $|j\rangle_{n_a}$ ($j = 0, \dots, 2^{n_a} - 1$) where j corresponds to the discretized possible values of $(x - x_c)^2/d_x^2$. We assume that n_a is sufficiently large for accurate discretization of such continuous values. We define the unitary adder via

$$\text{ADD}(|r\rangle_{n_a} \otimes |r'\rangle_{n_a} \otimes |0\rangle_{n_a}) = |r\rangle_{n_a} \otimes |r'\rangle_{n_a} \otimes |r + r'\rangle_{n_a}. \quad (\text{H6})$$

Explicit construction of an adder is known [52–54]. We define the exponential-function phase gate via

$$U_e(\theta)|r\rangle_{n_a} \equiv \exp(-ie^{-r}\theta)|r\rangle_{n_a} \quad (\text{H7})$$

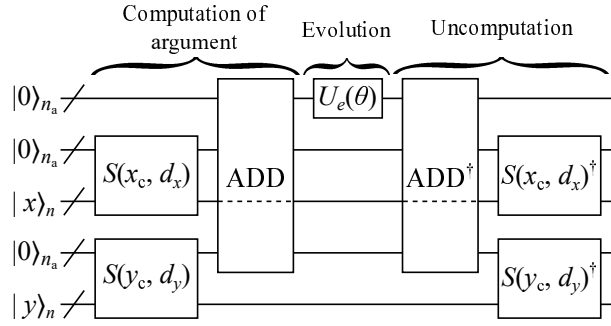


FIG. 14. Gaussian evolution circuit $\mathcal{C}_G(x_c, y_c, d_x, d_y, \theta)$ as a building block of $U_{\text{pot}}(\Delta t)$ for the double-well potential in Sect. III B.

with a predetermined circuit parameter θ . Although the unitary gates defined in Eqs. (H5), (H6), and (H7) may involve ancillary qubits other than the auxiliary registers, we do not write them explicitly in the equations for simplicity.

We define the Gaussian evolution circuit $\mathcal{C}_G(x_c, y_c, d_x, d_y, \theta)$ as shown in Fig. 14, which is made up of the three major parts: the computation of the argument, the evolution due to the potential, the uncomputation. One can easily confirm that this circuit implements the evolution for a Gaussian potential:

$$\begin{aligned} & \mathcal{C}_G(x_c, y_c, d_x, d_y, \theta) \left(|x^{(k)}\rangle \otimes |y^{(k')}\rangle \otimes (\text{initialized auxiliary qubits}) \right) \\ &= \exp \left(-i\theta \exp \left(-\frac{(x^{(k)} - x_c)^2}{d_x^2} - \frac{(y^{(k')} - y_c)^2}{d_y^2} \right) \right) |x^{(k)}\rangle \otimes |y^{(k')}\rangle \otimes (\text{initialized auxiliary qubits}). \end{aligned} \quad (\text{H8})$$

Thanks to the uncomputation part, which disentangles the auxiliary registers from the electronic register, we can discard the auxiliary registers safely [29]. Since the potential in the simulation is the sum of three Gaussian functions [see Eq. (33)], we can implement the potential-evolution as the consecutive Gaussian evolution circuits as

$$U_{\text{pot}}(\Delta t) = \mathcal{C}_G \left(\frac{L}{2}, \frac{L}{2}, \Delta_x, \Delta_y, V_p \Delta t \right) \mathcal{C}_G \left(\frac{L}{2} + a, \frac{L}{2}, \Delta, \Delta, V_0 \Delta t \right) \mathcal{C}_G \left(\frac{L}{2} - a, \frac{L}{2}, \Delta, \Delta, V_0 \Delta t \right). \quad (\text{H9})$$

The gate count for this implementation is thus given by

$$\begin{aligned} c(U_{\text{pot}}) &= 3c(\mathcal{C}_G) \\ &= 12c(S) + 6c(\text{ADD}) + 3c(U_e). \end{aligned} \quad (\text{H10})$$

That for the controlled U_{pot} can also be calculated similarly. Explicit construction of the circuit for $S(x_c, d_x)$ is possible since the arithmetic circuits for addition [52–54] and multiplication [55–57] are known. That of the circuit for $U_e(\theta)$ is also possible by approximating the exponential function as a piecewisely defined polynomial [26, 28]. We can thus evaluate Eq. (H10). The explicit construction of those circuits, however, goes beyond the scope of the present study.

-
- [1] K. v. Klitzing, G. Dorda, and M. Pepper, New method for high-accuracy determination of the fine-structure constant based on quantized hall resistance, *Phys. Rev. Lett.* **45**, 494 (1980).
[2] D. C. Tsui, H. L. Stormer, and A. C. Gossard, Two-dimensional magnetotransport in the extreme quantum limit, *Phys. Rev. Lett.* **48**, 1559 (1982).
[3] R. B. Laughlin, Anomalous quantum hall effect: An incompressible quantum fluid with fractionally charged ex-

- citations, *Phys. Rev. Lett.* **50**, 1395 (1983).
[4] H. L. Stormer, D. C. Tsui, and A. C. Gossard, The fractional quantum hall effect, *Rev. Mod. Phys.* **71**, S298 (1999).
[5] G. Murthy and R. Shankar, Hamiltonian theories of the fractional quantum hall effect, *Rev. Mod. Phys.* **75**, 1101 (2003).
[6] L. M. K. Vandersypen and I. L. Chuang, Nmr techniques for quantum control and computation,

- Rev. Mod. Phys.* **76**, 1037 (2005).
- [7] I. L. Chuang, L. M. K. Vandersypen, X. Zhou, D. W. Leung, and S. Lloyd, Experimental realization of a quantum algorithm, *Nature* **393**, 143 (1998).
- [8] M. A. Nielsen, E. Knill, and R. Laflamme, Complete quantum teleportation using nuclear magnetic resonance, *Nature* **396**, 52 (1998).
- [9] S. Somaroo, C. H. Tseng, T. F. Havel, R. Laflamme, and D. G. Cory, Quantum simulations on a quantum computer, *Phys. Rev. Lett.* **82**, 5381 (1999).
- [10] C. S. Yannoni, M. H. Sherwood, D. C. Miller, I. L. Chuang, L. M. K. Vandersypen, and M. G. Kubinec, Nuclear magnetic resonance quantum computing using liquid crystal solvents, *Applied Physics Letters* **75**, 3563 (1999), <https://doi.org/10.1063/1.125389>.
- [11] E. Knill, R. Laflamme, R. Martinez, and C.-H. Tseng, An algorithmic benchmark for quantum information processing, *Nature* **404**, 368 (2000).
- [12] L. M. K. Vandersypen, M. Steffen, G. Breyta, C. S. Yannoni, M. H. Sherwood, and I. L. Chuang, Experimental realization of shor's quantum factoring algorithm using nuclear magnetic resonance, *Nature* **414**, 883 (2001).
- [13] G. M. Leskowitz, N. Ghaderi, R. A. Olsen, and L. J. Mueller, Three-qubit nuclear magnetic resonance quantum information processing with a single-crystal solid, *The Journal of Chemical Physics* **119**, 1643 (2003), <https://doi.org/10.1063/1.1582171>.
- [14] S. Wiesner, Simulations of Many-Body Quantum Systems by a Quantum Computer, arXiv e-prints , quant-ph/9603028 (1996), [arXiv:quant-ph/9603028 \[quant-ph\]](https://arxiv.org/abs/quant-ph/9603028).
- [15] C. Zalka, Simulating quantum systems on a quantum computer, *Proceedings of the Royal Society of London. Series A: Mathematical, Physical and Engineering Sciences* **454**, 313 (1998), <https://royalsocietypublishing.org/doi/pdf/10.1098/rspa.1998.0167>.
- [16] I. Kassal, S. P. Jordan, P. J. Love, M. Mohseni, and A. Aspuru-Guzik, Polynomial-time quantum algorithm for the simulation of chemical dynamics, *Proceedings of the National Academy of Sciences* **105**, 18681 (2008), <https://www.pnas.org/content/105/48/18681.full.pdf>.
- [17] N. C. Jones, J. D. Whitfield, P. L. McMahon, M.-H. Yung, R. V. Meter, A. Aspuru-Guzik, and Y. Yamamoto, Faster quantum chemistry simulation on fault-tolerant quantum computers, *New Journal of Physics* **14**, 115023 (2012).
- [18] T. Kosugi, Y. Nishiyama, H. Nishi, and Y.-i. Matsushita, Imaginary-time evolution using forward and backward real-time evolution with a single ancilla: First-quantized eigensolver algorithm for quantum chemistry, *Phys. Rev. Research* **4**, 033121 (2022).
- [19] H. H. S. Chan, R. Meister, T. Jones, D. P. Tew, and S. C. Benjamin, Grid-based methods for chemistry simulations on a quantum computer, *Science Advances* **9**, eabo7484 (2023), <https://www.science.org/doi/pdf/10.1126/sciadv.abo7484>.
- [20] T. Kosugi, H. Nishi, and Y. Matsushita, Exhaustive search for optimal molecular geometries using imaginary-time evolution on a quantum computer, arXiv e-prints , arXiv:2210.09883 (2022), [arXiv:2210.09883 \[quant-ph\]](https://arxiv.org/abs/2210.09883).
- [21] M. P. Kaicher, S. B. Jäger, P.-L. Dallaire-Demers, and F. K. Wilhelm, Roadmap for quantum simulation of the fractional quantum hall effect, *Phys. Rev. A* **102**, 022607 (2020).
- [22] N. Watanabe and M. Tsukada, Finite element approach for simulating quantum electron dynamics in a magnetic field, *Journal of the Physical Society of Japan* **69**, 2962 (2000), <https://doi.org/10.1143/JPSJ.69.2962>.
- [23] K. Seki, Y. Otsuka, and S. Yunoki, Gutzwiller wave function on a quantum computer using a discrete hubbard-stratonovich transformation, *Phys. Rev. B* **105**, 155119 (2022).
- [24] Y. Mao, M. Chaudhary, M. Kondappan, J. Shi, E. O. Ilo-Okeke, V. Ivannikov, and T. Byrnes, Deterministic measurement-based imaginary time evolution, arXiv e-prints , arXiv:2202.09100 (2022), [arXiv:2202.09100 \[quant-ph\]](https://arxiv.org/abs/2202.09100).
- [25] D. S. Abrams and S. Lloyd, Simulation of many-body fermi systems on a universal quantum computer, *Phys. Rev. Lett.* **79**, 2586 (1997).
- [26] D. W. Berry, M. Kieferová, A. Scherer, Y. R. Sanders, G. H. Low, N. Wiebe, C. Gidney, and R. Babbush, Improved techniques for preparing eigenstates of fermionic hamiltonians, *npj Quantum Information* **4**, 22 (2018).
- [27] R. D. Somma, Quantum simulations of one dimensional quantum systems, arXiv e-prints , arXiv:1503.06319 (2015), [arXiv:1503.06319 \[quant-ph\]](https://arxiv.org/abs/1503.06319).
- [28] P. J. Ollitrault, G. Mazzola, and I. Tavernelli, Nonadiabatic molecular quantum dynamics with quantum computers, *Phys. Rev. Lett.* **125**, 260511 (2020).
- [29] M. A. Nielsen and I. L. Chuang, *Quantum Computation and Quantum Information: 10th Anniversary Edition*, 10th ed. (Cambridge University Press, New York, NY, USA, 2011).
- [30] G. Benenti and G. Strini, Quantum simulation of the single-particle schrödinger equation, *American Journal of Physics* **76**, 657 (2008), <https://doi.org/10.1119/1.2894582>.
- [31] T. Helgaker and P. Jørgensen, An electronic Hamiltonian for origin independent calculations of magnetic properties, *The Journal of Chemical Physics* **95**, 2595 (1991), <https://pubs.aip.org/aip/jcp/article-pdf/95/4/2595/8140048/2595-1>.
- [32] E. I. Tellgren, A. Soncini, and T. Helgaker, Nonperturbative ab initio calculations in strong magnetic fields using London orbitals, *The Journal of Chemical Physics* **129**, 10.1063/1.2996525 (2008), 154114, <https://pubs.aip.org/aip/jcp/article-pdf/doi/10.1063/1.2996525/1490000>.
- [33] G. Stefanucci and R. van Leeuwen, *Nonequilibrium Many-Body Theory of Quantum Systems* (Cambridge University Press, 2013).
- [34] M. Dimitrova, H. Fliegl, and D. Sundholm, The influence of heteroatoms on the aromatic character and the current pathways of b2n2-dibenzo[a,e]pentalenes, *Phys. Chem. Chem. Phys.* **19**, 20213 (2017).
- [35] D. Sundholm, M. Dimitrova, and R. J. F. Berger, Current density and molecular magnetic properties, *Chem. Commun.* **57**, 12362 (2021).
- [36] R. M. Parrish and P. L. McMahon, Quantum Filter Diagonalization: Quantum Eigendecomposition without Full Quantum Phase Estimation, arXiv e-prints , arXiv:1909.08925 (2019), [arXiv:1909.08925 \[quant-ph\]](https://arxiv.org/abs/1909.08925).
- [37] M. Motta, C. Sun, A. T. K. Tan, M. J. O'Rourke, E. Ye, A. J. Minnich, F. G. S. L. Brandão, and G. K.-L. Chan, Determining eigenstates and thermal states on a quantum computer using quantum imaginary time evolution, *Nature Physics* **16**, 205 (2020).
- [38] N. H. Stair, R. Huang, and F. A. Evange-

- lista, A multireference quantum krylov algorithm for strongly correlated electrons, *Journal of Chemical Theory and Computation* **16**, 2236 (2020), PMID: 32091895, <https://doi.org/10.1021/acs.jctc.9b01125>.
- [39] C. L. Cortes and S. K. Gray, Quantum krylov subspace algorithms for ground- and excited-state energy estimation, *Phys. Rev. A* **105**, 022417 (2022).
- [40] R. Meister and S. C. Benjamin, Resource-frugal Hamiltonian eigenstate preparation via repeated quantum phase estimation measurements, arXiv e-prints , arXiv:2212.00846 (2022), [arXiv:2212.00846 \[quant-ph\]](https://arxiv.org/abs/2212.00846).
- [41] V. Fock, Bemerkung zur quantelung des harmonischen oszillators im magnetfeld, *Zeitschrift für Physik* **47**, 446 (1928).
- [42] C. G. Darwin, The diamagnetism of the free electron, *Mathematical Proceedings of the Cambridge Philosophical Society* **27**, 86 (1931).
- [43] A. Bhuiyan and F. Marsiglio, Landau levels, edge states, and gauge choice in 2d quantum dots, *American Journal of Physics* **88**, 986 (2020), <https://doi.org/10.1119/10.0001703>.
- [44] P. A. Maksym, Eckardt frame theory of interacting electrons in quantum dots, *Phys. Rev. B* **53**, 10871 (1996).
- [45] J. Kainz, S. A. Mikhailov, A. Wensauer, and U. Rössler, Quantum dots in high magnetic fields: Calculation of ground-state properties, *Phys. Rev. B* **65**, 115305 (2002).
- [46] R. M. Abolfath, W. Dybalski, and P. Hawrylak, Theory of a two-level artificial molecule in laterally coupled quantum hall droplets, *Phys. Rev. B* **73**, 075314 (2006).
- [47] R. M. Abolfath and P. Hawrylak, Real space hartree-fock configuration interaction method for complex lateral quantum dot molecules, *The Journal of Chemical Physics* **125**, 034707 (2006), <https://doi.org/10.1063/1.2219447>.
- [48] H. Nishi, K. Hamada, Y. Nishiya, T. Kosugi, and Y.-i. Matsushita, Analyzing computational cost of probabilistic imaginary-time evolution method, arXiv e-prints , arXiv:2305.04600 (2023), [arXiv:2305.04600 \[quant-ph\]](https://arxiv.org/abs/2305.04600).
- [49] N. Klco and M. J. Savage, Minimally entangled state preparation of localized wave functions on quantum computers, *Phys. Rev. A* **102**, 012612 (2020).
- [50] C. S. Lent, Edge states in a circular quantum dot, *Phys. Rev. B* **43**, 4179 (1991).
- [51] A. Barenco, C. H. Bennett, R. Cleve, D. P. DiVincenzo, N. Margolus, P. Shor, T. Sleator, J. A. Smolin, and H. Weinfurter, Elementary gates for quantum computation, *Phys. Rev. A* **52**, 3457 (1995).
- [52] T. G. Draper, Addition on a Quantum Computer, arXiv e-prints , quant-ph/0008033 (2000), [arXiv:quant-ph/0008033 \[quant-ph\]](https://arxiv.org/abs/quant-ph/0008033).
- [53] T. G. Draper, S. A. Kutin, E. M. Rains, and K. M. Svore, A logarithmic-depth quantum carry-lookahead adder, arXiv e-prints , quant-ph/0406142 (2004), [arXiv:quant-ph/0406142 \[quant-ph\]](https://arxiv.org/abs/quant-ph/0406142).
- [54] A. Parent, M. Roetteler, and M. Mosca, Improved reversible and quantum circuits for Karatsuba-based integer multiplication, arXiv e-prints , arXiv:1706.03419 (2017), [arXiv:1706.03419 \[quant-ph\]](https://arxiv.org/abs/1706.03419).
- [55] L. A. B. Kowada, R. Portugal, and C. M. H. de Figueiredo, Reversible karatsuba's algorithm, *Journal of Universal Computer Science* **12**, 499 (2006).
- [56] A. Parent, M. Roetteler, and M. Mosca, Improved reversible and quantum circuits for Karatsuba-based integer multiplication, arXiv e-prints , arXiv:1706.03419 (2017), [arXiv:1706.03419 \[quant-ph\]](https://arxiv.org/abs/1706.03419).
- [57] S. Dutta, D. Bhattacharjee, and A. Chattopadhyay, Quantum circuits for toom-cook multiplication, *Phys. Rev. A* **98**, 012311 (2018).